J. Nonlinear Sci. Vol. 14: pp. 27–57 (2004)
DOI: 10.1007/s00332-003-0553-1

Journal of
Nonlinear
Science

© 2004 Springer-Verlag New York, LLC

Stability and Bifurcation Analysis of a Nonlinear DDE Model for Drilling

E. Stone[1] and S. A. Campbell[2]

[1] Department of Mathematics and Statistics, Utah State University, Logan, UT 84322-3900, USA
e-mail: stone@math.usu.edu

[2] Department of Applied Mathematics, University of Waterloo, Waterloo, Ontario, N2L 3G1, Canada

Received November 7, 2002; accepted September 24, 2003
Online publication February 20, 2004
Communicated by N. Sri Namachchivaya

Summary. We study a model for chatter in twist drills derived by Stone and Askari [*Dynam. Sys.*, 17, 1 (2002), 65–85], in which a linear vibration mode interacts with nonlinear cutting forces. This results in a delay differential equation describing an oscillator that is nonlinear in damping and with cross-terms in the damping and the delay. Linear stability analysis of the model with significant nonlinear terms is performed, and an analysis of the nonlinear stability of the primary Hopf bifurcation is observed. The latter is done via the construction, using symbolic algebra, of a two-dimensional centre manifold in the infinite dimensional space employing an algorithm developed by Campbell and Bélair [*SIAM J. Appl. Math.*, 54, 5 (1994), 1402–1424; and *Can. Appl. Math. Quart.*, 3, 2 (1995), 137–154]. Our analysis shows that the stability of the Hopf bifurcation depends on the type of vibration in question and on the cutting speed. These results are confirmed numerically and further bifurcations in the high-speed limit are also explored numerically, with tantalizing results that could be the basis of much future work.

Key words. delay differential equations, chatter, drilling, centre manifold reduction

1. Introduction

1.1. *The Chatter Instability in Metal Cutting*

When a metal cutting tool passes over a workpiece surface many times in succession, such as in a turning operation, it can be affected by irregularities in the material in a way that produces a sustained vibration, known as regenerative chatter. Since the forces on the tool depend on the chip thickness, and that thickness in turn depends on the present position of the tool and its position one revolution ago, regenerative chatter is modelled naturally by delay differential equations. This formulation first appeared in the (separate) work of Tobias [46] and Koenigsberger and Tlusty [23], who pioneered the stability analysis of regenerative chatter in the 1960s. Their results were very successful, and the now obvious requirement for delay equations in modeling chatter is due to their original insight. Another pioneer in developing the engineering mathematics of regenerative chatter is Gabor Stépán; a few of his papers on this topic can be found in [36], [37]. Nayfeh [29] introduced the use of perturbation methods to analyze the nonlinear stability of regenerative chatter, and his analysis has had experimental validation in the work of Pratt [31]. Other work on the nonlinear stability of chatter vibrations can be found in Kalmár, Stépán, and Moon [22].

Most extensively studied have been machining operations that involve orthogonal cutting, cutting where the tool is directed perpendicular to the cutting velocity. Milling is one example, and we reference here work by Tlusty and his students [45], and others [34], [35], and more recent work by Minis and Yanushevsky [27], Altintas and Budak [1], and Bayly, Halley et al. [2]. We are interested in particular in problems of chatter in drilling. Drilling is much more difficult to analyze than turning or milling, due to the complex geometry of the cutting surfaces. In an earlier paper [40] we examined the interaction of nonlinear friction on the tool and an axial-torsional vibrational mode seen in twist drills that is thought to be responsible for a certain type of chatter, one that leaves radial grooves in the bottom of a drilled hole. That work is complementary to work by Philip Bayly and his students [3], [4], [5], who consider the interaction of tool vibration with cutting forces in drilling. Other recent work in drilling has focused on deriving expressions for torque and thrust on the cutting edges of a drill [38], [39], vibration properties of drills in bending and torsion via finite element analysis [44], [32], [33], and experimental strategies for controlling chatter in drilling [42], [43], [13].

Here we extend the study in [40], which is limited to analyzing the linear stability of delay equations for the drill vibration modes, to the nonlinear analysis of the vibration that ensues. In particular, is the bifurcation to chatter subcritical or supercritical?

A subcritical bifurcation is important to identify, since it can turn sharp stability boundaries into blurred regions where the system may or may not go unstable, depending on the level of external noise or other perturbations. A subcritical Hopf bifurcation involves the collapse of an unstable limit cycle on the origin, causing the origin to lose stability at the bifurcation point. Prior to the bifurcation the unstable limit cycle acts as the boundary of the basin of attraction of the origin. If the phase point of the system is pushed beyond the limit cycle (either in position or velocity), the solution will be repelled away from the origin, leading to instability of the trivial solution for values of the bifurcation parameter *below* the bifurcation point. Subcritical bifurcations also lead to abrupt changes in the dynamics; once the bifurcation point is passed and the origin goes unstable, the solution must jump to some discontinuous branch in the parameter space, determined by the global features of the system. Therefore, unlike a supercritical Hopf bifurcation where the amplitude of the resulting oscillation grows smoothly up from zero, large amplitude oscillations can occur immediately upon crossing a subcritical Hopf bifurcation point. To classify the type of Hopf bifurcation here, we apply a symbolic algebra algorithm to approximate centre manifolds for delay equations which was developed by Bélair and Campbell [6], [9] to the equations derived for the drilling mode model in [40], to determine if the onset of instability predicted by the linearization of the model is subcritical or supercritical. We also extend the linear analysis in [40] by considering the effect of larger nonlinear coefficients on the stability diagrams, and by varying the structural damping.

Our main stability results depend on the type of vibration being considered, a vertical motion of the cutting tool, or a more complicated axial-torsional mode. The axial-torsional case exhibits very simple linear stability lobes, and the Hopf bifurcation is always subcritical. Including larger nonlinearities does affect the traditional case, however, creating loops from the stability lobes, with the primary Hopf bifurcation changing from subcritical to supercritical with increasing speed (decreasing delay). Studies of the high-speed limit, both numerical and analytical, uncover a a large-scale, long-period limit cycle whose period and amplitude increase as the limit is approached, and a degenerate Hopf bifurcation once the limit is attained.

In Section 1.2 we introduce the linear theory of chatter, followed by the exact form of the drilling model in Section 1.3 and the extended linear stability results in Section 2. The analysis of the criticality of Hopf bifurcation in the drilling model is presented in Section 3. In Section 4 some global results in the high-speed limit are presented. Section 5 discusses the results and open questions in the research. The appendix gives some background on the theory of delay differential equations, including details of the centre manifold calculations.

1.2. The Linear Theory of Chatter

As mentioned above, the phenomenon of regenerative chatter has been studied primarily with delay differential equations. In cutting processes that involve “turning,” the workpiece is rotated and moved into the cutting tool, which removes material in a thin shaving (a chip) in a corkscrew-like fashion. Thus the surface cut on one rotation becomes the surface to be cut on the next rotation. The thickness of the chip depends on the position of the tool at the time of the cut, and the position of the tool one revolution ago. The delay arises naturally as the time required for the workpiece to complete one revolution. This process can produce a self-sustained vibration when the tool hits a hard grain in the material and is forced up. Oscillations in the vertical position of the tool can then commence, which generate waviness in the cut surface. This waviness in turn generates oscillations of the cutting tool, and so on.

The problem of tool vibration in machining is usually simplified to the analysis of the excitation of vibration modes of the entire apparatus. The frequency and effective damping ratio of each mode is computed in laboratory tests, and generally only the lowest frequency modes are considered [46]. Most commonly considered is a mode that vibrates up and down perpendicular to the workpiece. The equation of motion for this vibration mode excited by a cutting force that depends on the thickness of the chip cut is

$$m\frac{d^2y}{dt^2} + c\frac{dy}{dt} + ky(t) = F(f + y(t) - y(t - T)). \tag{1}$$

Here $y(t)$ is the vertical position of the tool, F is the thrust force on the tool (in the y direction) and depends on the chip thickness, $(f + y(t) - y(t - T))$, where f is the

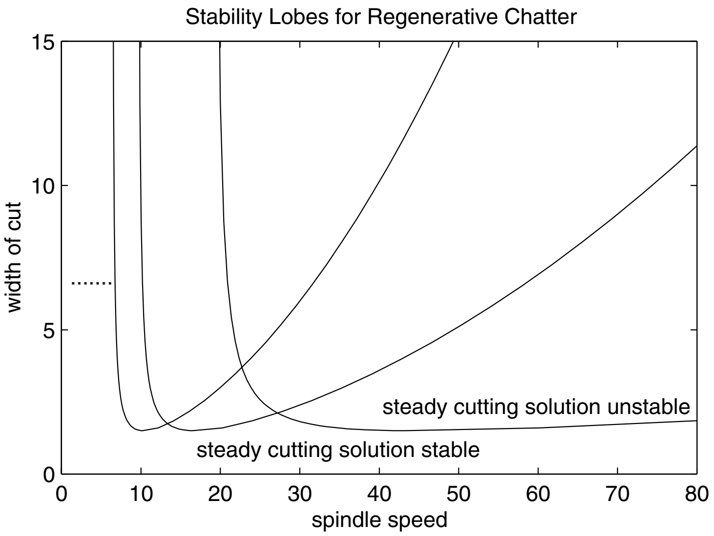

Fig. 1. Stability diagram for regenerative chatter. Steady cutting solution (the trivial solution) is stable in the region beneath the lobes.

feed (how much the material is moved toward the tool) per revolution and T is the time required for one revolution. Thus the basic description is a linear mass-spring system (m being the mass, and k the spring constant) with viscous damping (c), being driven by a forcing function with a delay. Using conventional techniques, we can create the stability diagram for regenerative chatter [46]; we show an example in Figure 1. The horizontal axis is spindle speed, which is inversely proportional to the delay, and the vertical axis is width of cut. Below the lobes the steady cutting solution is stable; upon crossing the boundary, a complex conjugate pair of eigenvalues of the steady state crosses the imaginary axis and the steady solution becomes an unstable spiral. Similar stability diagrams can be found in the papers of [7], [8], [10], [12], [21], which consider the damped harmonic oscillator with delayed position and/or velocity dependent feedback.

1.3. A Nonlinear Model for Chatter in Drilling

In [40] a model is developed for the interaction of an axial-torsional mode found in twist drills and the metal removal process. The vibrational modes of the drill are assumed to be primarily linear, with large inertia and stiffness, and small damping. The equation of motion in η, the modal amplitude, is hence

$$m\ddot{\eta} + c\dot{\eta} + k\eta = F_\eta, \tag{2}$$

where m is the inertial term, c is damping, and k is stiffness. The forcing function, F_η, is the projection of the cutting force $\mathbf{R}$ onto the vibration direction (see Figure 2); and $\mathbf{R}$ is determined from the Merchant-Oxley model of steady orthogonal cutting [25], [30]. We also incorporate nonlinear friction of the chip sliding on the rake face of the tool (through the friction coefficient λ), which can have the effect of actually *driving* the oscillation rather than damping it, by dragging the chip with the tool as it moves up.

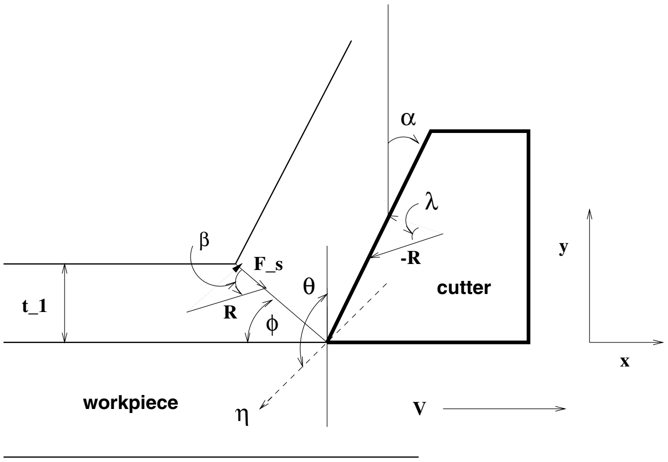

Fig. 2. Diagram of angles and forces for orthogonal cutting.

This friction force depends critically on the direction of the vibration mode in question, which is specified by the angle θ in Figure 2. Other parameters are t_1, the chip thickness; V, the cutting speed; ϕ, the shearplane angle; F_s, the force projected on the shearplane; and β, the angle the shearplane makes with $\mathbf{R}$ (ϕ, F_s, and β are used in the calculation of the cutting force; for more details, see [40]).

The cutting force F_η is a function of both η and $\dot{\eta}$, and takes the form

$$F(\eta, \dot{\eta}) = w\tau(t_1 - \eta\cos\theta)(p_0 + p_1\dot{\eta} + p_2\dot{\eta}^2). \tag{3}$$

Note that the force depends on the instantaneous chip thickness $(t_1 - \eta\cos\theta)$ and the penetration rate, $\dot{\eta}$. In our calculations we used values typical of drilling aluminum: $\alpha = .26$, $w = 6.35 \times 10^{-3}m$, $\tau = 276$ MPa, $k = 10^7 N/m$, $t_1 = 7.6 \times 10^{-5}m$, $V = 400 m/min$, and a friction model that yielded expansion coefficients p_0, p_1, and p_2 in decreasing asymptotic order. The p's depend on cutting speed, rake angle, and vibration angle in general. For the conditions considered in [40], both p_1 and p_2 are quite small for all angles, two to four orders of magnitude smaller than p_0 in most cases. For the axial-torsional mode, vibrations occur in the first and third quadrants, corresponding to a motion where the drill lengthens when it "unwinds," and a three-dimensional vibration analysis revealed that (approximately) $\theta = 1.38 = 79^\circ$. In this case both p_0 and p_1 are less than zero. For a vertical vibration, θ is zero, and p_0 and p_1 turn out to be positive for the rake angles we considered.

We can analyze regenerative chatter in our model by including the effect of chip thickness variation. This means that the chip thickness $t_1 - \eta\cos\theta$ becomes $t_1 - (\eta(t) - \eta(t-T))\cos\theta$, T being the time to complete one revolution of the workpiece. The equation for our vibration mode, after an appropriate rescaling, is then

$$\eta'' + \gamma\eta' + \eta - \beta(1 - (\eta - \eta_T)\cos\theta)(p_0 + \tilde{p}_1\eta' + \tilde{p}_2\eta'^2) = 0, \tag{4}$$

where $\eta_T = \eta(t-T)$. Note that $1/T$ is spindle speed in revolutions per unit time, and η is now the rescaled amplitude variable, and η' is the derivative with respect to the rescaled time variable. From the nondimensionalization we have $\beta = w\tau/k$ and $\tilde{p_1}$, $\tilde{p_2}$ are the rescaled p_1, p_2 (p_0 is left unchanged by the rescaling).

2. Linear Stability Diagrams

Referring to (4), we see that the steady state for the oscillator is $\eta = \beta p_0$, and we study neutral stability of this state by first linearizing the equation shifted to this fixed point, arriving at

$$z'' + (\gamma - \beta p_1)z' + z = -\beta p_0 \cos\theta (z - z_T), \tag{5}$$

where $z = \eta - \beta p_0$, and $z_T = \eta(T) - \beta p_0$. We find the curves in the parameter space $1/T, \beta$ where oscillatory solutions are neutrally stable, which partition the space into regions where the steady cutting solution is stable or unstable. To do so we substitute $z = e^{i\omega t}$ (the neutrally stable solution) into the equation and set the coefficients of the real and imaginary parts equal to zero. These two equations can be solved for β and T as functions of ω, namely,

$$T(\omega) = \frac{2}{\omega}(\arctan(\frac{1-\omega^2}{\Gamma\omega}) + n\pi), \qquad \beta(\omega) = \frac{1}{2p_0\cos\theta}\{\frac{(\Gamma\omega)^2}{\omega^2 - 1} + (\omega^2 - 1)\}. \tag{6}$$

We have set $\Gamma = \gamma - \beta p_1$, and for the following discussion assume that $\Gamma > 0$, to guarantee stability in the unforced case. We have also made approximations to arrive at these expressions. The calculation of p_0, p_1 depends on the spindle speed, i.e., $p_0 = p_0(T)$, $p_1 = p_1(T)$, so T has not been completely relegated to one expression. However, over the speeds we are considering, this variation is very small, so we approximate p_0 and p_1 by their value at the nominal spindle speed of 1000 rpm (corresponding to $V = 400$ m/min for the drill model).

In the cases examined in [40], another approximation is made. If it is assumed that $\beta p_1 << \gamma$, and $\Gamma \sim \gamma$, the expression (6) can be used directly to plot the curves parametrically in the $1/T, \beta$ plane. We plot the result in Figure 3. The distinct lobes are formed by taking different branches of the arctangent function ($n = 1, 2, \ldots$). In the region below the lobes, the steady cutting solution is stable, and by continuous dependence on parameters all the eigenvalues must still have negative real part. As a lobe is crossed out of this region, a pair of complex conjugate eigenvalues crosses the imaginary axis and the steady solution is now unstable. We show here the lobes for $p_0 \cos\theta$ negative and positive. The positive $p_0 \cos\theta (= 1)$ diagram is the traditional milling-type chatter stability diagram seen, for instance, in Moon and Johnson [28], and is plotted by varying ω through values greater than the natural frequency of the oscillator (which in this case is normalized to 1). The vertical asymptote for each lobe is located at $\frac{1}{2n\pi}$ so that the lobes accumulate on the vertical axis as $n \to \infty$. For $p_0 \cos\theta (= -1)$ negative, to achieve positive values of β in the stability diagram, ω must be varied between zero and the natural frequency of the oscillator. Bayly has observed this phenomenon in axial-torsional vibrations of twist drills in laboratory experiments [3]. He found that the onset chatter oscillation will have a frequency *less* than the natural frequency of the vibration mode, which is in contrast to the traditional case where the onset chatter frequency will be greater than the natural frequency. For his experimentally

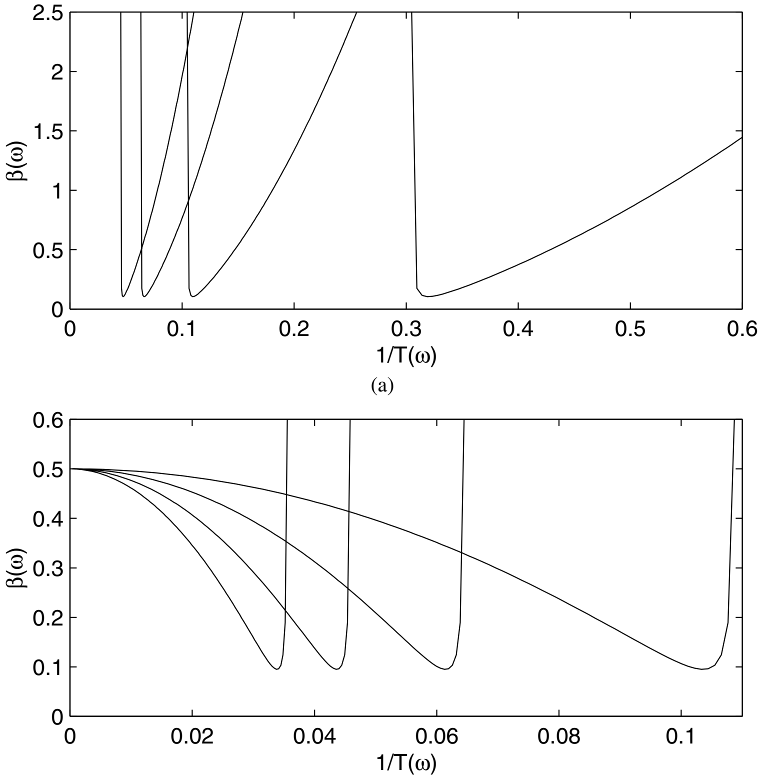

(a)

(b)

Fig. 3. Stability diagram for (a) $p_0 \cos\theta = 1$, (b) $p_0 \cos\theta = -1$. The top diagram is equivalent to the one presented in Figure 1. The trivial solution is unstable in the region above the boundaries, and stable below.

determined equation, the coefficient multiplying $(z - z_T)$ on the right-hand side of (5) is positive, which puts it in the category of $p_0 \cos\theta < 0$. The lobes for this case are shown in Figure 3(b), and also accumulate on the vertical axis as $n \to \infty$. The cusps occur near the vertical asymptote of curves, that is, as $\omega \to \omega_o(= 1)$. The spindle speed limits on $\frac{\omega_o}{2\pi n}$ at the vertical asymptote, as it does in the traditional models. This quantifies the machinist's lore that to avoid chatter the spindle speed can be tuned to integer multiples of the natural frequency of the vibrational mode being excited.

If we now no longer assume that $p_1\beta << \gamma$ (which it may very well not be), the expressions for the boundaries become more complex. The equation for β in (6) becomes a quadratic in β, namely,

$$p_1^2\omega^2\beta^2 - ((\omega^2 - 1)(2p_0 \cos\theta) + 2\gamma p_1\omega^2)\beta + (\gamma^2\omega^2 + (\omega^2 - 1)^2) = 0. \quad (7)$$

And the equation for T becomes

$$T(\omega) = \frac{2}{\omega}(\arctan(\frac{1 - \omega^2}{(\gamma - \beta p_1)\omega}) + n\pi). \quad (8)$$

The roots of the quadratic must be found and substituted into the expression for $T(\omega)$ before a point on the boundary can be computed. Furthermore there will be ranges of ω for which there are no real or positive solutions to the quadratic for β, and those must be identified and excluded. Since $T(\omega)$ contains a term that has $\Gamma = \gamma - \beta p_1$ in the denominator, the points where Γ vanishes must be located as well, for the arctangent jumps from one branch to another at these places. We present here two case studies with order 1 parameters, one typical of a vibration in the vertical direction, and another with parameters computed for an axial-torsional vibration. Specifically, case I: $p_0 \cos\theta = 0.8, \quad p_1 = 0.2$ (traditional/milling case with vertical vibration); and case II: $p_0 \cos\theta = -0.8, \quad p_1 = -0.4$ (axial-torsional case).

From the form of the solution to the quadratic for β, we can draw some conclusions about the stability boundaries for the two different cases. First, the solution to the quadratic can be written

$$\beta_{+,-} = \frac{(\omega^2-1)p_0\cos\theta + \gamma p_1\omega^2 \pm \sqrt{\begin{matrix}[(\omega^2-1)p_0\cos\theta + \gamma p_1\omega^2]^2 \\ -[\gamma^2\omega^2 + (\omega^2-1)^2]p_1^2\omega^2\end{matrix}}}{p_1^2\omega^2},$$

and the ranges of ω where a real, positive solution exists can be identified by evaluating the discriminant. When $\omega = 1$ the discriminant vanishes, for all other parameters values. For the axial-torsional case, positive solutions for β occur for values of ω between zero and 1, and for the traditional case, for values of ω greater than 1, similar to what was observed in the simplified situation studied initially. Other zeros of the discriminant further reduce the range of allowable ω in each case, so that positive real branches are found for $\omega \in [0, 0.79]$ for the axial-torsional parameters, and $\omega \in [1, 4.5]$ (approximately), in the traditional case, with $\gamma = 0.5$, in both. The right-hand boundary of these intervals we'll call ω_c, where ω_c is less than 1 in the axial-torsional case, and greater than 1 in the traditional case.

The most notable difference in the stability diagrams for the two cases is the presence of closed loops in the traditional case vs. no loops in the axial-torsional case; see Figures 4 and 5. Close into the lower boundary the loops are not apparent (Figure 4, top), the diagram looks like the usual overlapping lobes, but taking a larger view reveals the loops. We note here that the region above the loops will have a spectrum that contains one complex conjugate pair of eigenvalues, while the region within the loops will have varying numbers depending on the exact situation of the overlapping branches. Plotting the plus and minus branches of β vs. ω in the traditional case illustrates why the loops occurs; see Figures 6 and 7. Here the two branches in the solution for β join up to form a loop, which forces the parametric curves in the stability diagram to also cycle in β as ω is varied, returning to the same β value, though $\frac{1}{T}$ increases monotonically with increasing ω. For the axial-torsional case the loops are not formed, since $\beta \to \infty$ as $\omega \to 0$ on the relevant branch.

To make these statements more concrete, consider the $\omega \to 0$ limit for the axial-torsional case. All curves begin on the β_- branch, at the point $(0, -\frac{1}{2p_0\cos\theta})$, and switch to β_+ at ω_c. For β_- it is easy to see that the $\lim_{\omega\to 0}\beta_- = -\frac{1}{2p_0\cos\theta}$ by substituting $\omega = 0$ into the original quadratic equation for β and solving for β. This works only for

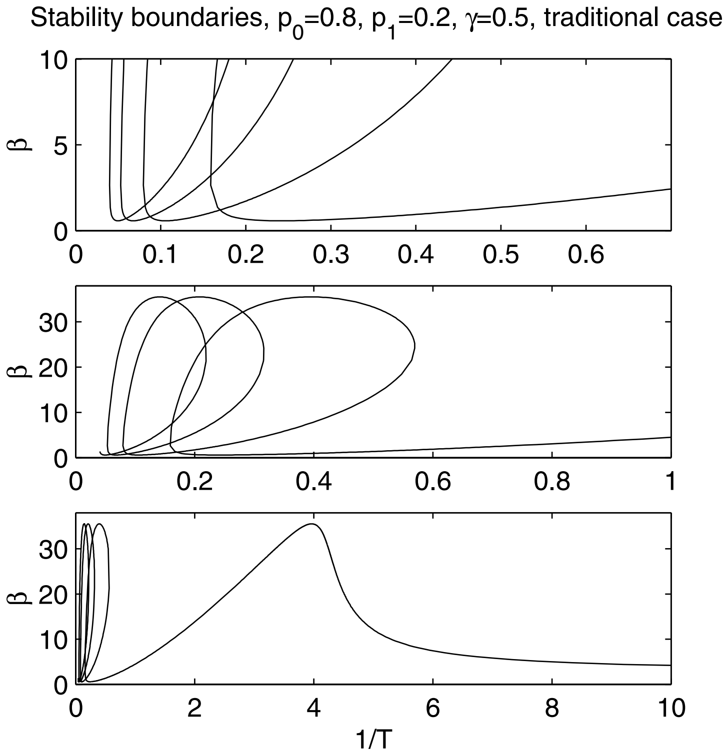

Fig. 4. Stability diagram for the traditional case: $\gamma = 0.5$, $p_0 \cos\theta = 0.8$, $p_1 = 0.2$. Moving from top to bottom zooms out from the area near the lower part of the boundary for lower cutting speeds. The trivial solution is unstable in the region above the boundaries, and stable below.

the β_- branch, where the limit is indeterminant (it can be shown directly by a repeated application of L'Hôpital's rule). The β_+ root increases to ∞ as ω is decreased from ω_c to zero, and T evaluated with this β root tends to ∞, so $1/T$ tends to zero, giving the curve $\beta(\omega)$ a vertical asymptote on the $\omega = 0$ axis. The location of the cusps in the diagram, or crossing points of the stability curves, is no longer near the point of vertical tangency (which occurs when $\omega = \omega_c$), and cannot be identified as such.

In the traditional case, the limit $\omega \to 1$ for the $n = 0$ branch determines the value of β when $\frac{1}{T} \to \infty$, and can be shown to be $\frac{\gamma}{p_1}$. Therefore the lower boundary for large $\frac{1}{T}$ increases with increasing γ, as would be expected. For smaller, more physically realistic cutting speeds, the minimum of the loops determines the lower point of the boundary, and they occur close to where neighboring loops cross and form cusps. These points are close to where the β_+ and β_- part of a given branch of the arctangent meet (located where the loop has a vertical tangent), which occurs in the limit $\omega \to 1$ for $n > 0$. For a given n, the $\lim_{\omega\to 1} T = \frac{1}{2\pi n}$, so the position of the cusps is essentially unchanged from the $\beta p_1 << \gamma$ case.

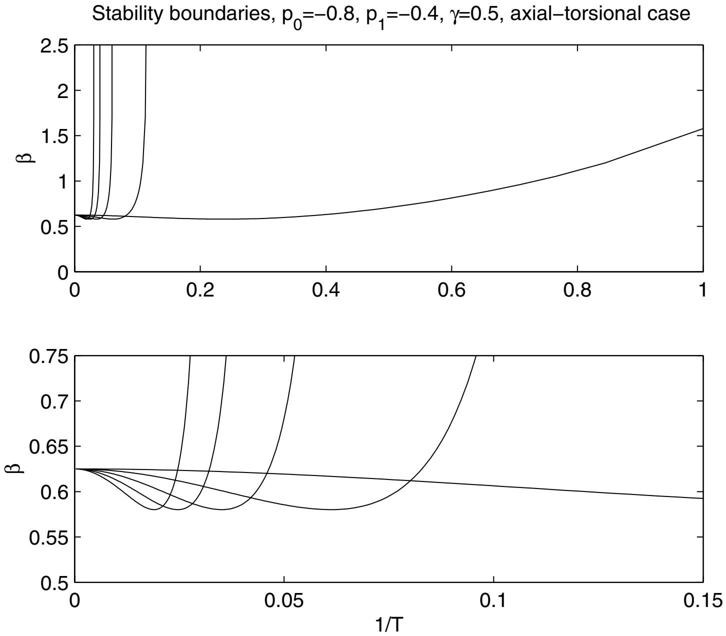

Fig. 5. Stability diagram for axial-torsional vibration: $\gamma = 0.5,\quad p_0 \cos\theta = -0.8,\quad p_1 = -0.4$. Moving from bottom to top zooms in on the area near the lower part of the boundary for lower cutting speeds. The trivial solution is unstable in the region above the boundaries, and stable below.

It is interesting to consider the effect of increasing damping on these diagrams, and for the axial-torsional case a common result in these sorts of delay equations occurs: The branches pull up in such a way as to eliminate the "lobes," and the $n = 0$ branch becomes the first stability boundary for all $\frac{1}{T}$. See Figure 8. Note that all the curves meet when $\omega = 0$, at the point $(0, -\frac{1}{2p_0\cos\theta})$, which is independent of γ. Whether the curves will intersect and form lobes, or pull through as in the $\gamma = 2.0$ case, can be studied by considering again solutions to the quadratic equation for β. When the branches do not intersect, it is necessary to have a unique ω for a given β, for if this is true, that ω will yield a T value that increases with increasing n, causing the lobes to separate by an amount determined by the jump in T value as n is incremented. If, however, more than one ω value gives a certain β, the branches can cross. Comparing the plots of β vs. ω, in Figure 7, we see this difference: When $\gamma = 0.5$, there is a region where $\omega(\beta)$ (flipping the axis in the figure) is multivalued, but when $\gamma = 2.0$ there is not. A necessary but not sufficient condition for this can be derived by considering the form of $\omega(\beta)$, which is determined from the same quadratic equation for β, which is also a quadratic in ω^2. It is straightforward to show that there is at least one positive solution for ω^2 if $\beta > -\frac{1}{2p_0\cos\theta}$, and for that to be the only solution it is also possible to show that either $p_0\cos\theta \le -1$, or $p_0\cos\theta > -1$ and $\gamma > \sqrt{2(1 + p_0\cos\theta)}$. This gives a lower bound on the value of γ for which only single values of ω can occur for a given β value, and for $p_0\cos\theta = -0.8,\quad p_1 = -0.4$ it is approximately 0.63.

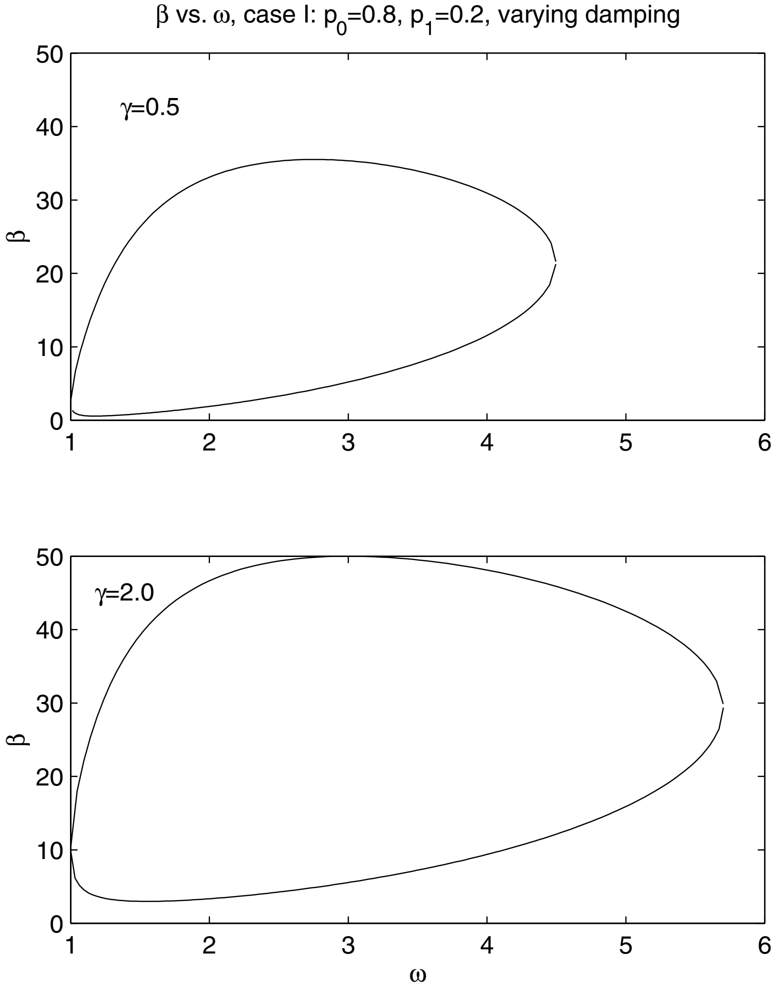

Fig. 6. β vs. ω for traditional vibration mode: $\gamma = 0.5$, $p_0 \cos\theta = 0.8$, $p_1 = 0.2$. Closed loops in this plane indicate loops in the stability diagram.

Another way to determine when pull-through occurs is to find numerically the second derivative of β with respect to ω, evaluated in the limit as $\omega \to 0$. It can be shown (using repeated applications of L'Hôpital's rule to determine the limit) that the first derivative is always zero at $\omega = 0$, independent of γ, so the sign of the second derivative will determine if the curve initially dips below $\frac{1}{2p_0 \cos\theta}$, which means that the branch must cross that value again as ω increased, since it ultimately increases to meet the other branch. Determining the second derivative and evaluating it in the limit as $\omega \to 0$ is most easily done by a combination of symbolic and numerical calculations for different values of γ, since the limit again involves multiple applications of L'Hôpital's rule. For instance, for $p_0 \cos\theta = -0.8$, $p_1 = -0.4$ the critical value of γ, for which $\beta''(\omega = 0) = 0$, is $\gamma = 0.75$. Note that this is above the lower bound computed in the preceding paragraph.

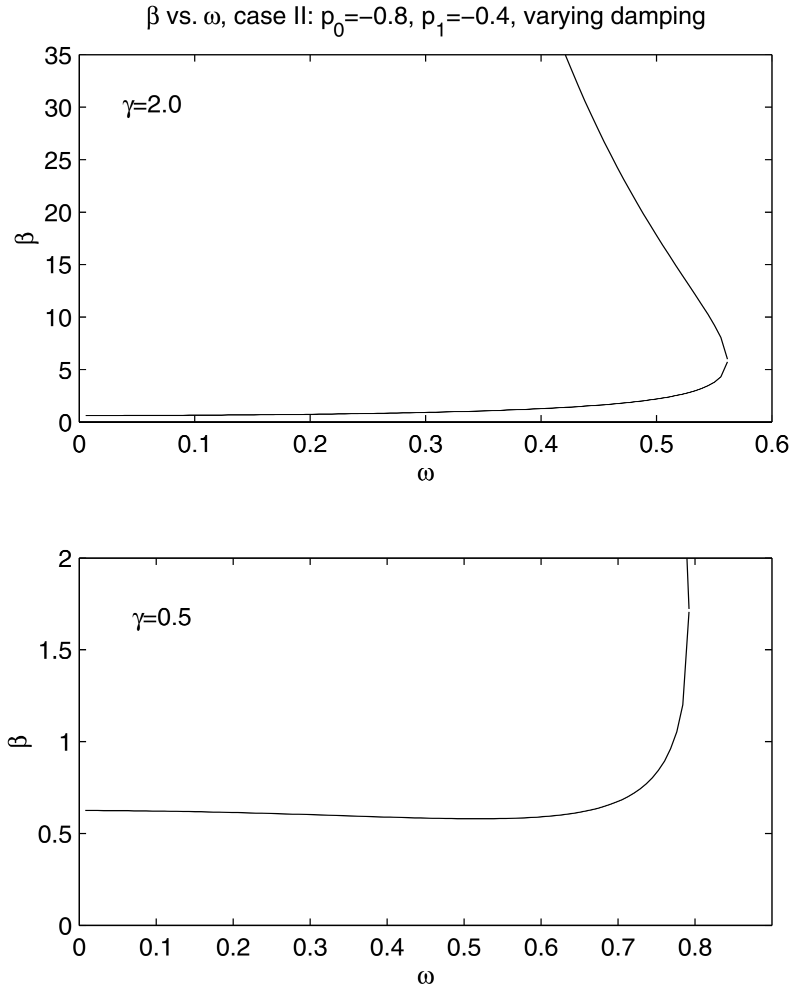

Fig. 7. β vs. ω for the axial-torsional vibration mode, $p_0 \cos\theta = -0.8, \quad p_1 = -0.4$, varying γ. No loops will be present in the stability diagrams, and for increased damping the lower lobes disappear.

For the traditional case, the effect of increased damping is illustrated in Figure 9. In the limit as the cutting speed $1/T$ goes to ∞ (on the $n = 0$ branch), the value of β limits on $\frac{\gamma}{p_1}$, so that boundary moves up as γ increases. This limit occurs as $\omega \to 1$, which means the point $(\frac{1}{T} = \frac{1}{2\pi n}, \beta = \frac{\gamma}{p_1})$ on the other branches (close to each cusp) moves up with γ as well. The location of the minima of the lobes is independent of the branch of the arctangent and can be determined by symbolic calculation. A graph of this minimum vs. γ is shown in Figure 10, and not surprisingly it increases with increasing γ.

To summarize this section, we can say that relaxation of the criteria $\beta p_1 << \gamma$ in the model changes the form of the linear stability boundaries. For questions concerning the onset of chatter, the most important change would be the shifting of the cusps

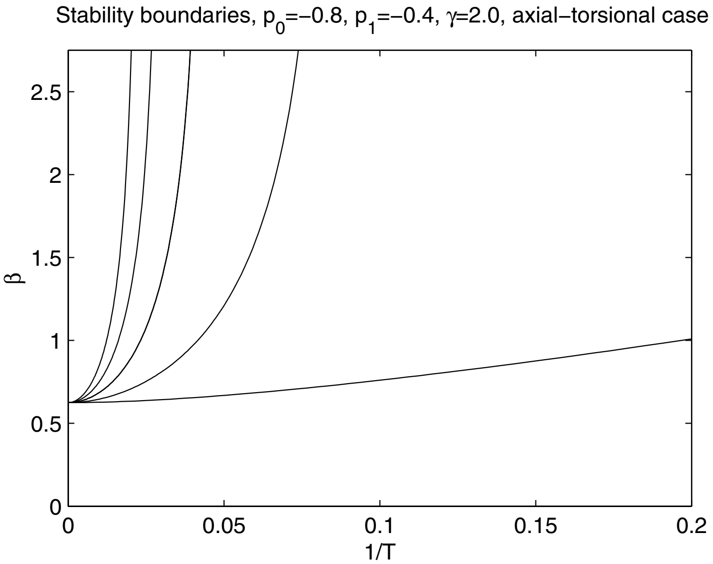

Fig. 8. Stability diagram for the axial-torsional vibration mode: $p_0 \cos\theta = -0.8$, $p_1 = -0.4$, with increased damping, $\gamma = 2.0$. The branches pull up to remove the lower boundary lobing.

in the axial-torsional case. The loops found in the traditional case, while interesting mathematically, would not affect the primary instability seen at the lower boundary. In both cases increasing structural damping causes this lower boundary to move up, increasing the size of the region where the trivial solution is stable. In the next section we take up the nonlinear analysis when the lowest stability boundary is crossed, a complex conjugate pair of eigenvalues pass through the imaginary axis, and the trivial solution loses stability in a Hopf bifurcation.

3. Hopf Bifurcation Analysis

The previous section described curves, in the T, β parameter space, where the equilibrium solution of (4) loses stability. At each point on these curves, the characteristic equation

$$\lambda^2 + (\gamma - \beta p_1)\lambda + (1 + \beta p_0) - \beta p_0 e^{-\lambda T} = 0$$

of the linearization (5) of (4) has a pair of pure imaginary roots, and the rest of the roots have negative real parts. As discussed in Appendix A, it is straightforward to check that the DDE (4) satisfies the conditions for a Hopf bifurcation to occur as, for example, β is increased through a point on these curves with T held fixed.

To study the criticality of the Hopf bifurcation, it is useful to reformulate the model as follows. Shifting the equilibrium in (4) to the origin and rewriting the result as a vector equation, we obtain

$$\mathbf{x}'(t) = A_0\mathbf{x}(t) + A_1\mathbf{x}(t - T) + \mathbf{f}(\mathbf{x}(t), \mathbf{x}(t - T)), \tag{9}$$

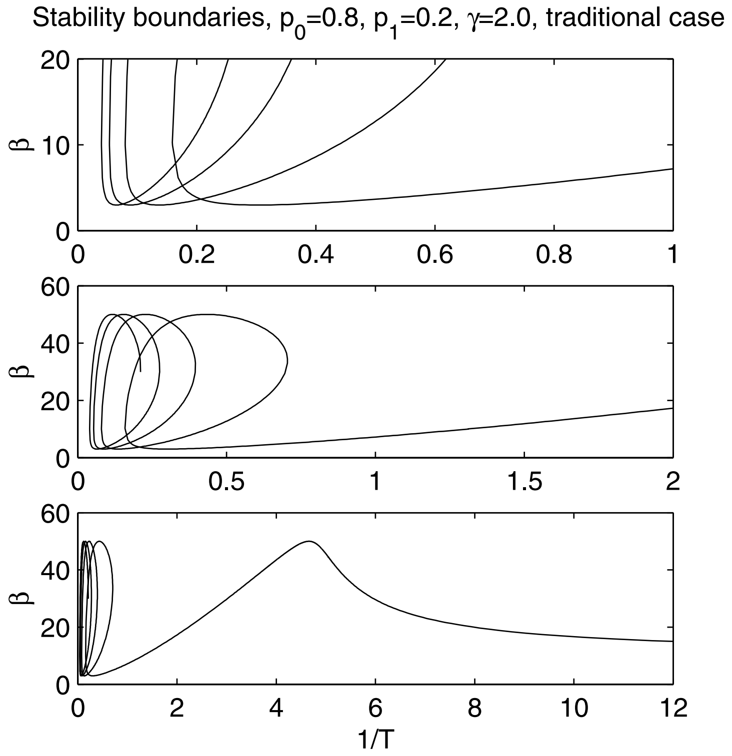

Fig. 9. Stability diagram for the traditional vibration mode with larger damping: $\gamma = 2.0, \quad p_0 \cos\theta = 0.8, \quad p_1 = 0.2$. Moving from top to bottom zooms out from the area near the lower part of the boundary for lower cutting speeds. The trivial solution is unstable in the region above the boundaries, and stable below.

where

$$\mathbf{x}(t) = \begin{bmatrix} x(t) \\ x'(t) \end{bmatrix} = \begin{bmatrix} \eta(t) - \beta p_0 \\ \eta'(t) \end{bmatrix},$$

$$A_0 = \begin{bmatrix} 0 & 1 \\ -1 - \beta \tilde{p}_0 & \beta p_1 - \gamma \end{bmatrix}, \qquad A_1 = \begin{bmatrix} 0 & 0 \\ \beta \tilde{p}_0 & 0 \end{bmatrix}, \tag{10}$$

$\tilde{p}_0 = p_0 \cos(\theta)$, and

$$\mathbf{f} = \begin{bmatrix} 0 \\ \beta p_2 x'(t)^2 - \beta \cos(\theta)(x(t) - x(t-T))(p_1 x'(t) + p_2 x'(t)^2) \end{bmatrix}. \tag{11}$$

The linearization of this equation about the trivial solution is

$$\mathbf{x}'(t) = A_0 \mathbf{x}(t) + A_1 \mathbf{x}(t-T). \tag{12}$$

It can be shown [20] that the solution space of equations such as (9) and (12) is infinite dimensional, and thus it is common to take as the phase space for the equation

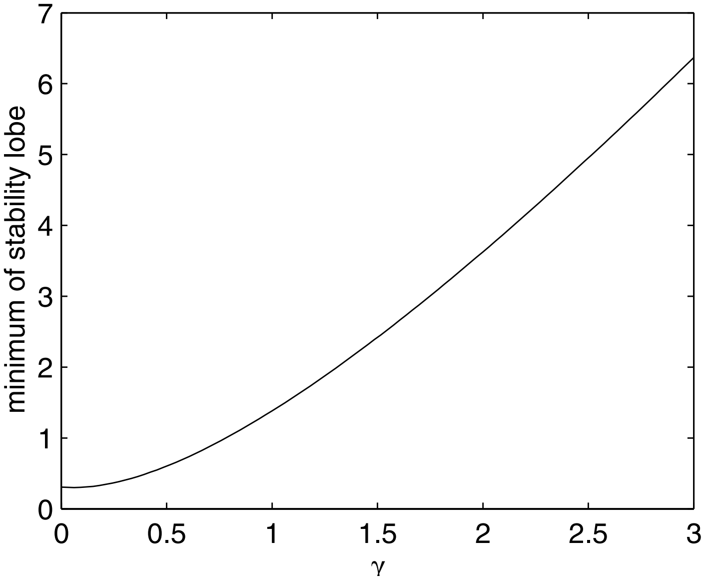

Fig. 10. Dependence of minimum lobe value on γ. Traditional vibration mode: $p_0 \cos\theta = 0.8, \quad p_1 = 0.2$. Increasing damping increases the size of the stable region beneath the lobes.

$\mathcal{C} \overset{def}{=} C([-T, 0], \mathbb{R}^2)$, the space of continuous functions mapping the interval $[-T, 0]$ into $\mathbb{R}^2$. This is accomplished by defining the function

$$\mathbf{x}_t(\sigma) \overset{def}{=} \mathbf{x}(t + \sigma), \quad -T \leq \sigma \leq 0,$$

to be the "phase point" at time t. Note that this represents the value of the state $\mathbf{x}$ at time t together with its past history to $t - T$.

Despite the infinite dimensionality of this phase space, many of the properties of solutions of delay differential equations such as (9) are similar to those for ordinary differential equations [20]. In particular, at a Hopf bifurcation point, there exists a two-dimensional centre manifold in the solution space. Further, if all the other roots of the characteristic equation of the linearization about the equilibrium have negative real parts, then this manifold is attracting, and the long-term behaviour of solutions to the nonlinear delay differential equation is well approximated by the flow on this manifold. As discussed in [15], [16], [48], the criticality of the Hopf bifurcation can be determined by studying the evolution of solutions on the centre manifold. We note that since the manifold is finite dimensional, this evolution will be described by a system of ordinary differential equations. In this section we will outline the steps needed to find this system of ordinary differential equations. Details of the computations and the theory behind them can be found in Appendix A.

Since we are primarily interested in bifurcations that affect the observed behaviour of the system, we will restrict ourselves to the Hopf bifurcations that occur along the curves (or parts of curves) of Section 2 which form the boundary of the region of stability of the equilibrium solution. At points along such curves, the trivial solution of (9) has a two-dimensional "centre eigenspace," N, with basis

$$\Phi(\sigma) = [\phi_1(\sigma), \phi_2(\sigma)] = \begin{bmatrix} \cos(\omega\sigma) & \sin(\omega\sigma) \\ -\omega\sin(\omega\sigma) & \omega\cos(\omega\sigma) \end{bmatrix}, \tag{13}$$

and an infinite dimensional "stable eigenspace" S. The corresponding centre manifold is given by

$$M_f = \{\phi \in \mathcal{C} \mid \phi = \Phi\mathbf{u} + \mathbf{h}(\mathbf{u})\},$$

where $\mathbf{u} = [u_1, u_2]^T$ are coordinates on N and $\mathbf{h}(\mathbf{u}) \in S$; and solutions to the DDE (9) on M_f are given by $\mathbf{x}_t(\sigma) = \Phi(\sigma)\mathbf{u}(t) + \mathbf{h}(\sigma, \mathbf{u}(t))$. This can be expressed as

$$\begin{aligned} \mathbf{x}_t(\sigma) \;=\; & \begin{bmatrix} \cos(\omega\sigma)u_1(t) + \sin(\omega\sigma)u_2(t) \\ -\omega\sin(\omega\sigma)u_1(t) + \omega\cos(\omega\sigma)u_2(t) \end{bmatrix} \\ & + \begin{bmatrix} h^1_{11}(\sigma)u_1(t)^2 + h^1_{12}(\sigma)u_1(t)u_2(t) + h^1_{22}(\sigma)u_2(t)^2 \\ h^2_{11}(\sigma)u_1(t)^2 + h^2_{12}(\sigma)u_1(t)u_2(t) + h^2_{22}(\sigma)u_2(t)^2 \end{bmatrix} + \mathrm{O}(\|\mathbf{u}\|^3), \end{aligned}$$

where the $h^i_{jk}(\sigma)$ are found by solving an ODE boundary value problem as described in Appendix A.

The dynamics on the centre manifold are given by the evolution in time of the coordinates $u_1(t),\ u_2(t)$. This is governed by the system of ODEs,

$$\begin{matrix} \dot{u}_1 = \omega u_2 + \Psi_{12}(0)(f_{11}u_1^2 + f_{12}u_1u_2 + f_{22}u_2^2 + f_{111}u_1^3 + f_{112}u_1^2u_2 + f_{122}u_1u_2^2 + f_{222}u_2^3) \\ \dot{u}_2 = -\omega u_1 + \Psi_{22}(0)(f_{11}u_1^2 + f_{12}u_1u_2 + f_{22}u_2^2 + f_{111}u_1^3 + f_{112}u_1^2u_2 + f_{122}u_1u_2^2 + f_{222}u_2^3) \end{matrix} + \mathrm{O}(\|\mathbf{u}\|^4),$$

where

$$\begin{aligned} \Psi(0) = & \frac{2\omega^2}{D} \\ & \times \begin{bmatrix} (\gamma - \beta p_1)(\beta\tilde{p}_0 + 1)T + 2\omega^2 + (\gamma - \beta p_1)^2 & (\beta\tilde{p}_0 + 1 - \omega^2)T + (\gamma - \beta p_1) \\ \omega[((\gamma - \beta p_1)^2 - (\beta\tilde{p}_0 + 1) + \omega^2)T + \gamma - \beta p_1] & \omega[(\gamma - \beta p_1)T + 2] \end{bmatrix}, \end{aligned} \tag{14}$$

with

$$\begin{aligned} D \;=\; & (5 + 2(\gamma - \beta p_1)T)\omega^4 + \big[\beta^2\tilde{p}_0^2T^2 \\ & + 2(\gamma - \beta p_1)(\beta\tilde{p}_0 + 1)T + 2(\gamma - \beta p_1)^2 - 2(\beta\tilde{p}_0 + 1)\big]\omega^2 + 2\beta\tilde{p}_0 + 1, \end{aligned}$$

and $\tilde{p}_0 = p_0\cos(\theta)$. The f_{jk} and f_{ijk} are functions of the parameters β, T, γ, θ, p_0, p_1, p_2, the Hopf frequency ω, and the centre manifold coefficients $h^i_{jk}(0)$ and $h^i_{jk}(-T)$. For example,

$$\begin{aligned} f_{11} \;&=\; 0, \\ f_{12} \;&=\; \omega\beta p_1\cos(\theta)(\cos(\omega T) - 1), \\ f_{22} \;&=\; \omega\beta(\omega p_2 - p_1\cos(\theta)\sin(\omega T), \\ f_{222} \;&=\; \beta[-\omega^2 p_2\cos(\theta)\sin(\omega T) + (2\omega p_2 \\ &\qquad - p_1\cos(\theta)\sin(\omega T))h^2_{22}(0) + \omega p_1\cos(\theta)(h^1_{22}(-T) - h^1_{22}(0))], \end{aligned}$$

where

$$h^1_{22}(0) = (1-\omega^2)\frac{p_1}{2p_0}\Psi_{12}(0) - \frac{\omega}{3}\left(\beta p_2 + (\gamma - \beta p_1)\frac{p_1}{p_0}\right)\Psi_{22}(0) - \frac{C_6}{2} + C_2, \text{ etc.,}$$

and the C_j are constants calculated as described in Appendix A.

Using the result given in [18, p. 152], it is easily shown that the criticality of the Hopf bifurcation is determined by the sign of the following quantity:

$$\begin{aligned} a = {} & \frac{1}{8}\left[\Psi_{12}(0)(3f_{111} + f_{122}) + \Psi_{22}(0)(f_{112} + 3f_{222})\right] \\ & - \frac{1}{8\omega}\left[(\Psi_{12}(0)^2 - \Psi_{22}(0)^2) f_{12}(f_{11} + f_{22}) + 2\Psi_{12}(0)\Psi_{22}(0)(f^2_{22} - f^2_{11})\right]. \end{aligned} \tag{15}$$

Using the expressions for the f_{ij}, f_{ijk}, this becomes

$$\begin{aligned} a = {} & \frac{1}{8}\beta^2\omega\nu p_1(\cos(\omega T) - 1)(-p_2\omega + \nu p_1 \sin(\omega T))\Psi_{12}(0)^2 \\ & + \frac{1}{4}\beta^2\omega[\nu^2 {p_1}^2(\cos(\omega T)^2 - 1) + \omega p_2(2\nu p_1 \sin(\omega T) - \omega p_2)]\Psi_{12}(0)\Psi_{22}(0) \\ & - \frac{1}{8}\beta^2\omega\nu p_1(\cos(\omega T) - 1)(-p_2\omega + \nu p_1 \sin(\omega T))\Psi_{22}(0)^2 \\ & - \frac{1}{8}\beta[\nu p_2\omega^2(1 - \cos(\omega T)) + \nu p_1\omega(h^1_{12}(0) - h^1_{12}(-T)) \\ & + 3\nu p_1(1 - \cos(\omega T))h^2_{11}(0) + (\nu p_1 \sin(\omega T) - 2\omega p_2)h^2_{12}(0) \\ & + \nu p_1(1 - \cos(\omega T))h^2_{22}(0)]\Psi_{12}(0) \\ & - \frac{1}{8}\beta[3\nu p_2 \sin(\omega T)\omega^2 + \nu p_1\omega(h^1_{11}(0) - h^1_{11}(-T)) \\ & + 3\nu p_1\omega(h^1_{22}(0) - h^1_{22}(-T)) + (\nu p_1 \sin(\omega T) - 2p_2\omega)h^2_{11}(0) \\ & + \nu p_1(1 - \cos(\omega T))h^2_{12}(0) + 3(\nu p_1 \sin(\omega T) - 2p_2\omega)h^2_{22}(0)]\Psi_{22}(0), \end{aligned}$$

where $\nu = \cos\theta$.

We have evaluated this coefficient along the boundary of the stability regions for both the traditional case (shown in Figures 4 and 9) and the axial-torsional case (shown in Figures 5 and 8). In the traditional case, the Hopf bifurcation is subcritical for large values of T (small turning speeds), then switches to supercritical at some intermediate value of T and remains so for small values of T (large turning speeds). Increasing the damping moves the point of change of criticality to smaller values of T. The results are illustrated in Figures 11 and 12. Light lines denote subcritical Hopf bifurcation and dark lines supercritical. In the axial-torsional case, the Hopf bifurcation is always subcritical.

To verify these predictions, we carried out numerical simulations on the full model (9) (i.e. (4) with the equilibrium shifted to zero) for various parameter values. The simulations were performed using the package XPPAUT [14] which uses a fourth-order Runge-Kutta integrator adapted for delay differential equations. In both cases, the simulations

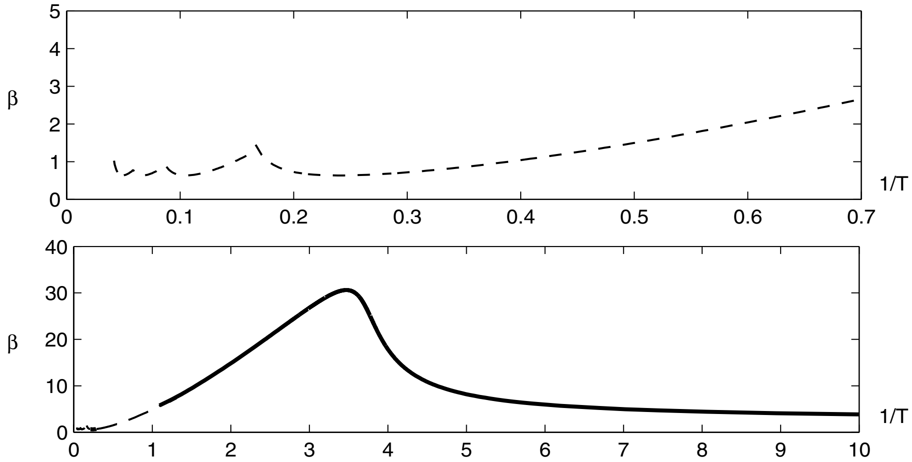

Fig. 11. Stability boundary showing criticality of Hopf bifurcation. The top diagram is a blowup of the bottom diagram, and hatched lines indicate a subcritical Hopf bifurcation, solid lines a supercritical Hopf. Traditional case with $p_0 \cos(\theta) = 0.8,\ p_1 = 0.2,\ p_2 = 0.1,\ \gamma = 0.5$.

confirmed our predictions. Figures 13 to 15 show simulations for various turning speeds for the traditional case. Figure 13 shows typical simulations for low turning speeds (large delay, T). Before the bifurcation, some initial conditions lead to solutions that converge to zero (solid line) and others lead to solutions that grow without bound (dashed line), indicating the presence of an unstable object which we postulate is a periodic orbit. After the bifurcation, all initial conditions lead to solutions that grow without

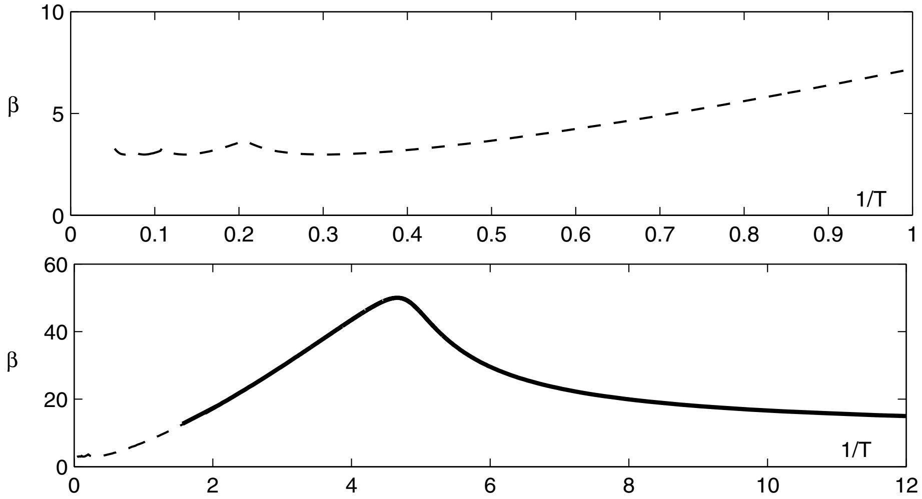

Fig. 12. Stability boundary showing criticality of Hopf bifurcation. The top diagram is a blowup of the bottom diagram, and hatched lines indicate a subcritical Hopf bifurcation, solid lines a supercritical Hopf. Traditional case with $p_0 \cos(\theta) = 0.8,\ p_1 = 0.2,\ p_2 = 0.1,\ \gamma = 2.0$.

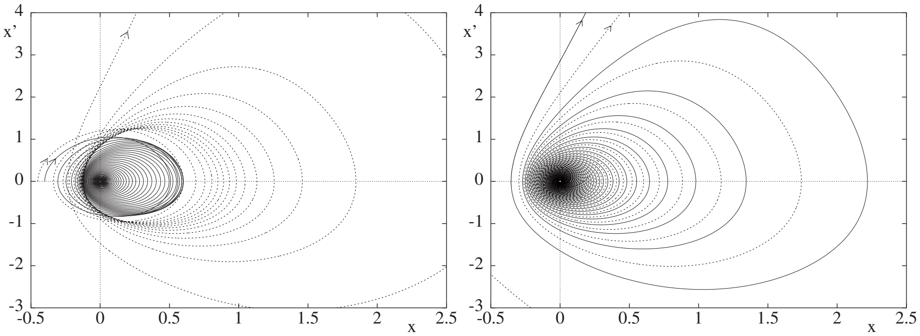

(a) Before Hopf bifurcation, $\beta = 3.4$ (b) After Hopf bifurcation, $\beta = 3.8$

Fig. 13. Numerical simulations of (9) showing a subcritical Hopf bifurcation for the traditional vibration mode. Parameter values: $\gamma = 2$, $T = 2$, $p_0 = 0.8$, $p_1 = 0.2$, $p_2 = 0.1$, $\theta = 0$. Initial conditions: $x(t) = x_0 \cos 2.2t$, $x'(t) = -2.2x_0 \sin 2.2t$, $-T \le t \le 0$; (a) $x_0 = -0.4$ (solid), -0.45 (dashed); (b) $x_0 = 0.01$ (solid), -0.01 (dashed). The Hopf bifurcation occurs when $\beta \approx 3.663$.

bound. This behaviour is consistent with a subcritical Hopf bifurcation. Figure 14 shows typical simulations for high turning speeds (small delay). Before the bifurcation, all initial conditions lead to solutions that converge to zero. After the bifurcation, all initial conditions lead to solutions which converge to a stable limit cycle. This behaviour is consistent with a supercritical Hopf bifurcation. Figure 15 shows a simulation at an intermediate speed, near a point where the criticality switches. Before the bifurcation the behaviour is similar to that for a subcritical Hopf bifurcation, i.e., some initial conditions lead to solutions that converge to zero (solid line), while others lead to solutions that grow without bound (dashed line), indicating the presence of an unstable object (probably

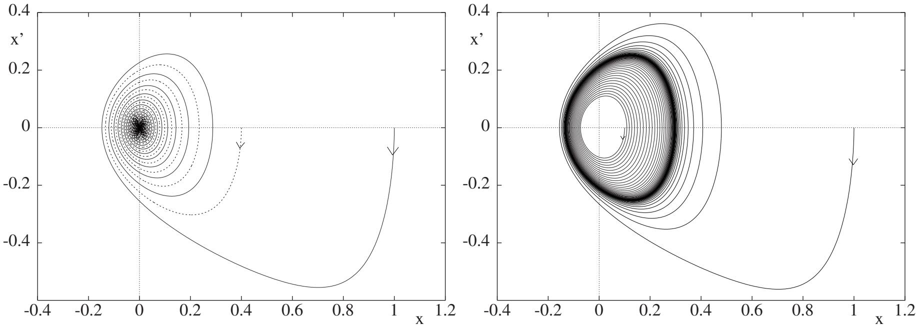

(a) Before Hopf bifurcation, $\beta = 29$ (b) After Hopf bifurcation, $\beta = 30$

Fig. 14. Numerical simulations of (9) showing a supercritical Hopf bifurcation for the traditional vibration mode. Parameter values: $\gamma = 2$, $T = 1/6$, $p_0 = 0.8$, $p_1 = 0.2$, $p_2 = 0.1$, $\theta = 0$. Initial conditions: $x(t) = x_0$, $x'(t) = 0$, $-T \le t \le 0$; (a) $x_0 = 0.4$ (dashed), 1 (solid); (b) $x_0 = 0.1$, 1.1. The Hopf bifurcation occurs when $\beta \approx 29.593$.

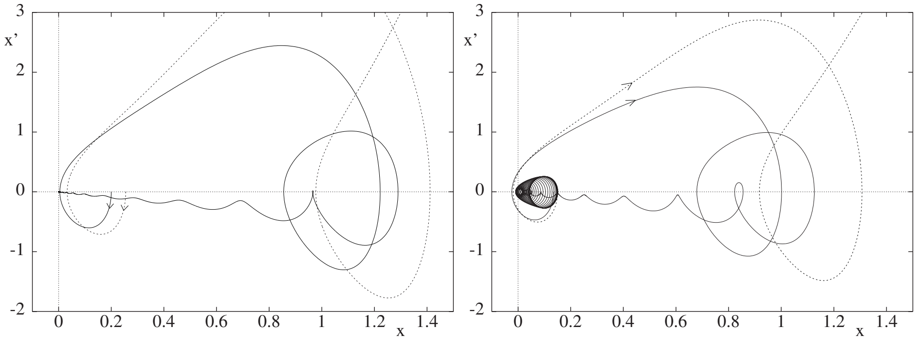

(a) Before Hopf bifurcation, $\beta = 43$ (b) After Hopf bifurcation, $\beta = 44$

Fig. 15. Numerical simulations of (9) showing a supercritical Hopf bifurcation near a change of criticality for the traditional vibration mode. Parameter values: $\gamma = 2$, $T = 0.25$, $p_0 = 0.8$, $p_1 = 0.2$, $p_2 = 0.1$, $\theta = 0$. Initial conditions: $x(t) = x_0 \cos 5t,\ x'(t) = -5x_0 \sin 5t,\ -T \leq t \leq 0$; (a) $x_0 = 0.2$ (solid), 0.255 (dashed); (b) $x_0 = 0.135$ (solid), 0.15 (dashed). The Hopf bifurcation occurs when $\beta \approx 43.45$.

a periodic orbit). After the Hopf bifurcation, some initial conditions lead to solutions that converge to a stable limit cycle (solid line), while others lead to solutions that grow without bound (dashed line), indicating that the unstable object persists after the Hopf bifurcation. This behaviour is consistent with a supercritical Hopf bifurcation near a point of change of criticality where the higher (i.e., fourth and bigger) order terms are destabilizing. See [18, pp. 358–360] and [17], [41]. For the axial-torsional case, simulations with any turning speed appear qualitatively like Figure 13, i.e., they are consistent with a subcritical Hopf bifurcation.

4. Exploring the High-Speed Stability Limit

We discovered that the stability and dynamics in the high-speed limit shapes what is seen at more moderate speeds, that is, for larger delays. In the high-speed limit, as T goes to zero, the equations are no longer delay equations and can be analyzed by conventional techniques. We outline here the results of this investigation and connect it to the overall dynamics and stability analysis presented in the previous sections.

The high-speed stability limit can be reached only in the traditional case, where the $n = 0$ branch extends out to infinity in the $1/T$ direction, with a horizontal asymptote at $\frac{\gamma}{p_1}$ as $\omega \to 1$, as mentioned in Section 2. In the axial-torsional (AT) case, the $n = 0$ branch approaches a vertical asymptote as $\omega \to 0$ with $\frac{1}{T} = \frac{|p_0|}{-p_1}$, also mentioned in Section 2. All other branches bend backward toward the β axis as β is increased, so the largest value of $\frac{1}{T}$ achieved in the stability boundaries in the axial-torsional case is $\frac{|p_0|}{-p_1}$. This means that there exists a large stable region to the right of the $n = 0$ curve in the axial-torsional case, which can be explained by examining the sign of the linear damping term, $\gamma - \beta p_1$. In the axial-torsional case p_1 is negative, so increasing β increases the

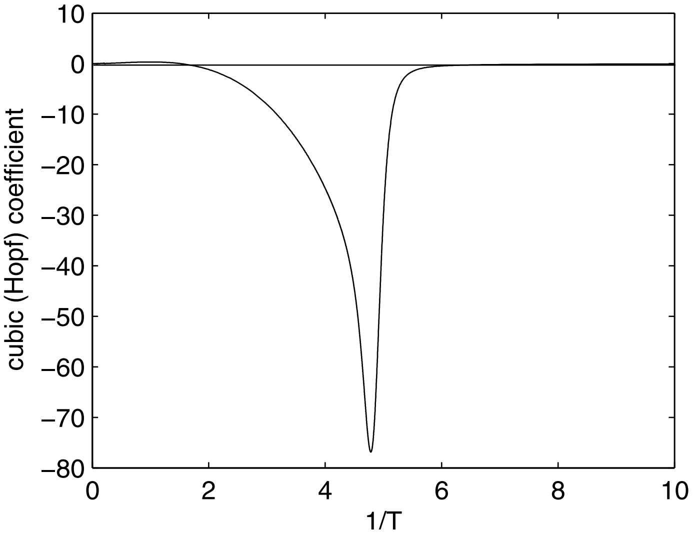

Fig. 16. The cubic coefficient from the Hopf criticality calculation along the linear stability boundary with increasing speed ($1/T$) in the traditional case with $\gamma = 2.0$. The region of subcriticality (though weak) can be seen for lower speeds, and the behaviour of the coefficient as speed is increased. In the limit as $1/T \to \infty$ the coefficient is zero.

linear structural damping and that counteracts the destabilizing effect of the delayed forcing.

In the traditional case, the linear damping term can change sign when $\gamma = \beta p_1$, since p_1 is positive. In the high-speed limit, the stability boundary corresponds to this value: The origin goes unstable when $\beta = \gamma p_1$, the horizontal asymptote for the $n = 0$ branch. We can further investigate the dynamics by considering the full equation of motion in the $T \to 0$ limit. Then $\eta = \eta_T$ and the equation of motion becomes

$$\eta'' + \gamma\eta' + \eta - \beta(p_0 + \tilde{p}_1\eta' + \tilde{p}_2\eta'^2) = 0. \tag{16}$$

Shifting the origin to the fixed point at $\eta = \beta p_0$, the equation is

$$z'' + (\gamma - \beta\tilde{p}_1)z' + z - \beta\tilde{p}_2 z'^2 = 0, \tag{17}$$

($z = \eta - \beta p_0$) a nonlinear oscillator with a Hopf bifurcation at $\beta = \frac{\gamma}{p_1}$.

Computing the criticality coefficient for the Hopf bifurcation using traditional techniques (see for instance [18]) yields $a = 0$, meaning that higher order terms would need to be generated to further determine the stability. This is consistent with the result in the delayed case as $T \to 0$, where the Hopf bifurcation coefficient is small and tends toward zero in the limit. See Figure 16 for an illustration: The coefficient is plotted as a function of increasing speed along the $n = 0$ branch.

An example of the vector field and solutions prior to the Hopf is plotted in Figure 17. Some solutions escape to infinity in the positive y direction; the nullcline $y' = 0$ indicated in the diagram with a hatched line gives some indication of the basin of attraction of the

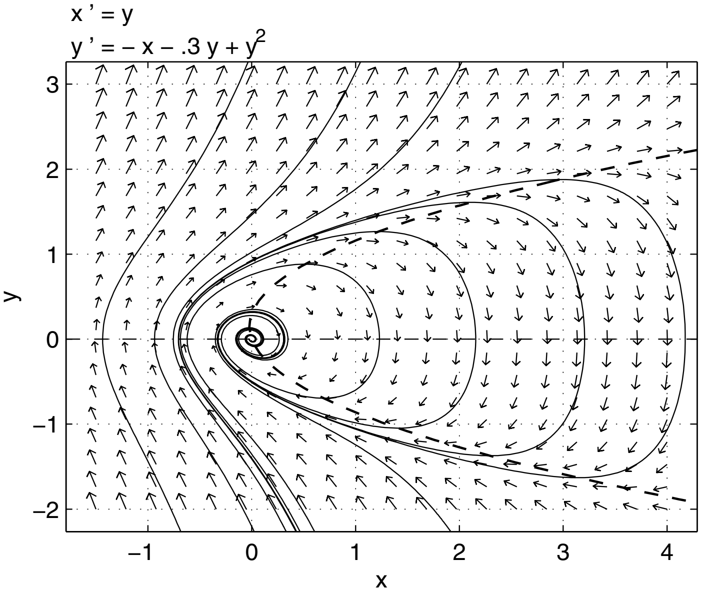

Fig. 17. Phase plane and direction field for the nonlinear system that results in the $T \to 0$ limit, $\gamma = 2.3$, $\tilde{p}_1 = 0.2$, $\tilde{p}_2 = 0.1$, $\beta = 10.0$. Isocline $y' = 0$ is indicated by the hatched line.

origin. After the (degenerate) Hopf bifurcation, all solutions escape to infinity. The shape of the orbits that decay to the origin in the nondelayed system is similar to that of the limit cycle created in the supercritical Hopf in the T nonzero case (see Figure 14). Moving out in the direction of increasing speed along the stability boundary, the small limit cycle created in the Hopf bifurcation becomes unstable to a large limit cycle that grows increasingly larger with increasing speed. Presumably the smaller cycle collides with an unstable manifold in a global bifurcation as β is increased away from the boundary. An illustration of this phenomenon is shown in Figure 18. There we can see the progression from a small stable cycle (a), to a small stable cycle with a transient loop around the large cycle (b), to the large cycle with a transient loop around the small cycle (c), to an even larger large cycle (d), with increasing speed, but identical initial conditions. The large limit cycle increases in size and period as the speed is increased, similar to heteroclinic bifurcations in nonlinear systems without delay. Further research into this limit would be very interesting, and is a relatively unexplored area of DDE research: how to analyze global bifurcations in general, and those which involve the limit to a nondelayed equation in particular.

5. Discussion and Future Work

In this paper we have studied the linear bifurcation structure of a nonlinear model for the axial-torsional chatter seen in twist drills, and considered the nonlinear stability of the

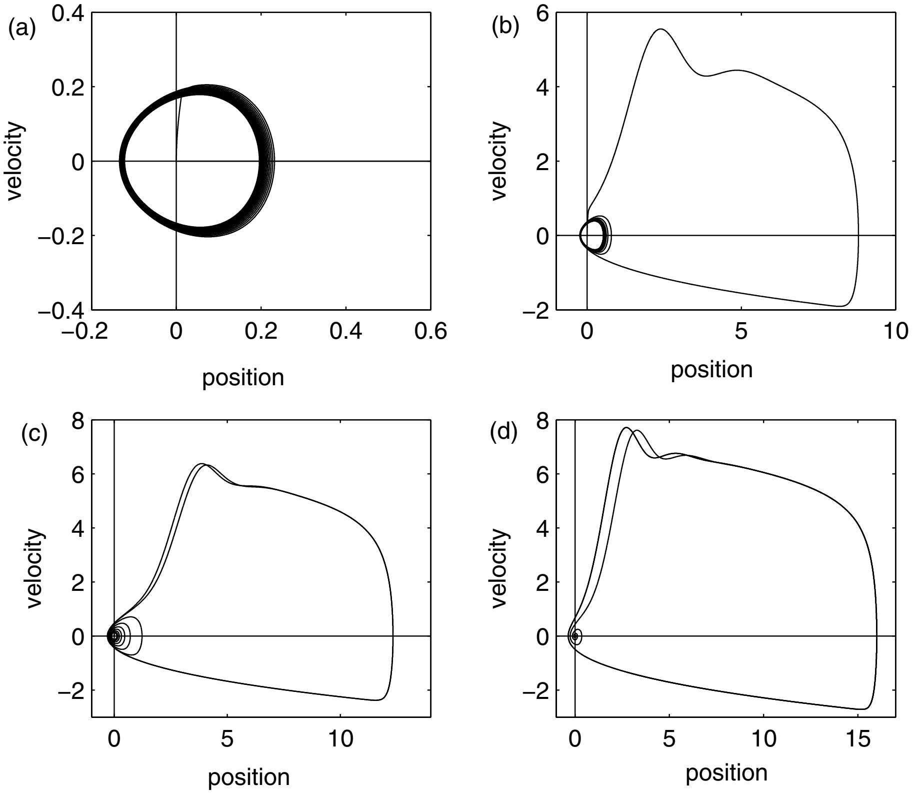

Fig. 18. Phase planes for increasing speed (decreasing delay T) to illustrate the global bifurcation. All cases have $\gamma = 2.0$, $p_0 = 0.8$, $\tilde{p}_1 = 0.2$, $\tilde{p}_2 = 0.1$, and identical initial conditions. The parameters β and T are as follows: (a) $\beta = 25$, $T = 0.15$, (b) $\beta = 23$, $T = 0.14$, (c) $\beta = 20$, $T = 0.12$, (d) $\beta = 20$, $T = 0.11$. Flow is always clockwise around the cycle and the initial conditions are $x(t) = x_0 \cos 4.5t,\ x'(t) = x_0 \sin 4.5t,\ -T \leq t \leq 0$.

resulting limit cycles. Inclusion of the nonlinear terms, if not asymptotically small, can significantly change the structure of the stability diagram presented in feed vs. cutting speed parameter space, depending on the details of the linear vibration mode (the angle at which the cutter vibrates). A significant feature of the stability diagrams remains unchanged from the linear model: the presence of cusps where feed can be increased past the baseline required for steady cutting, if the speed is chosen well. This naturally can increase efficiency for a given cutting operation.

Whether the onset of chatter seen at these boundaries is subcritical or supercritical has grave consequences for the implementation of such stability curves in machining operations. If the instability is subcritical, the stability threshold is reduced by an amount dependent on the perturbations present in the system and the details of the dynamics away from the fixed point. Such perturbations could include hitting a hard grain in the material where the amplitude tool is forced up out of the basin of attraction of the steady cutting solution. Variation in cutting speed or chip load might also contribute to perturbations that might push the system into instability. An unstable limit cycle would exist that separates the attracting f.p. (below the threshold) from a region where chatter will occur. Any perturbation to the system that pushes it past this boundary in phase space would generate an oscillation. The stability lobes turn from sharp boundaries into fuzzy regions where the probability of encountering chatter is significant, and these regions extend below the sharp boundary, diminishing the effective region of stability of the steady solution. Our analysis indicates that the Hopf bifurcation that occurs when the stability boundaries are crossed is always subcritical in the axial-torsional case. In the traditional case, it is primarily supercritical for high machining speeds, and then switches to subcritical for lower speeds. Increasing the damping increases the speed at which the switch of criticality takes place. Numerical investigations near parameter values where the switch occurs suggest the existence of another unstable limit set, which is consistent with being near a point of change of criticality of a bifurcation, where the smaller order parameters become important in the dynamics.

In the high-speed machining limit, the delay differential equation becomes an ordinary differential equation that can be analyzed by conventional techniques. We see that the vector field for this system influences the structure of the flow in the small delay case, and that the criticality coefficient for the Hopf bifurcation is zero, indicating degeneracy. Numerical simulations of the delay differential equation in this limit show a global bifurcation leading to a large-scale limit cycle whose period increases with increasing speed, reminiscent of a heteroclinic bifurcation in nondelayed systems. Such bifurcations in delay differential equations are not well understood, and this system provides an example for future research in that area.

In future work we plan to investigate the primary bifurcations of this nonlinear model with the constraints on the coefficients relaxed further to allow them to depend explicitly on speed. This complicates the form of the stability lobes in the feed-speed space, as well as the criticality of the instability seen on the boundary. Most models of regenerative chatter have been developed to study the instability seen when the cutting width is increased. A more natural parameter for drilling is cutting depth, and an initial investigation into models scaled around cutting depth rather than width shows a significantly altered and more complicated linear stability diagram. We plan to explore both the linear and nonlinear aspects of bifurcations seen as cutting depth is increased. Further investigations of damping mechanisms in metal cutting are leading to the development of an oscillator model with delayed feedback where the frictional damping is discontinuous, depending on whether the tool is moving down into the material or away. The form of this model is similar to a physiological model of the pupil light reflex [24, 26] and we plan to study a general situation that can be extended to both cases.

Appendix A: Background on Delay Differential Equations

Consider the nonlinear drilling model expressed in vector form,

$$\mathbf{x}'(t) = A_0\mathbf{x}(t) + A_1\mathbf{x}(t-T) + \mathbf{f}(\mathbf{x}(t), \mathbf{x}(t-T)), \tag{18}$$

where A_0, A_1, and $\mathbf{f}$ are as defined in (10)–(22) of Section 3.

To pose an initial value problem at $t = t_0$ for this DDE, one must specify the value of $x(t)$ not just at $t = t_0$, but on the whole interval $[t_0 - T, t_0]$. Thus an appropriate initial condition is

$$\mathbf{x}(t_0 + \sigma) = \zeta_0(\sigma), \quad -T \le \sigma \le 0, \tag{19}$$

where $\zeta_0 : [-T, 0) \to \mathbb{R}^2$ is a given function. It can be shown [20] that under certain conditions on ζ_0 and $\mathbf{f}$ (e.g., ζ_0 continuous) there exists a unique solution to the initial value problem (18)–(19) which is defined and continuous on a (maximal) interval $[t_0 - T, \beta),\ \beta > 0$. We will assume that ζ_0 is continuous and that $\mathbf{f}$ satisfies the necessary conditions.

To define an appropriate phase space for the solutions of the DDE, we make the following definition:

$$\mathbf{x}_t(\sigma) \overset{def}{=} \mathbf{x}(t + \sigma), \quad -T \le \sigma \le 0.$$

Note that the initial condition can now be expressed as $\mathbf{x}_{t_0} = \zeta_0$ and that $\mathbf{x}_t$ will be a continuous mapping from $[-T, 0] \to \mathbb{R}^2$ for each $t \in [t_0, \beta)$.

With this in mind, it is usual [20] to take the phase space for (18) to be the Banach space $\mathcal{C} \overset{def}{=} C([-T, 0], \mathbb{R}^2)$ of continuous mappings from $[-T, 0]$ into $\mathbb{R}^2$, equipped with the norm

$$\|\zeta\|_T = \sup_{\sigma \in [-T,0]} \|\zeta(\sigma)\|,$$

where $\|\cdot\|$ is the usual Euclidean norm on $\mathbb{R}^2$. We can then define the flow for the DDE as a mapping on $\mathcal{C}$ which takes the initial function ζ_0 into the function $\mathbf{x}_t$.

The equation (18) for $x(t)$ can be expressed as a *functional differential equation* (FDE)

$$\mathbf{x}'(t) = L(\mathbf{x}_t) + \mathbf{F}(\mathbf{x}_t), \tag{20}$$

where $L : \mathcal{C} \to \mathbb{R}^2$ is a linear operator defined by

$$L(\zeta(\sigma)) = A_0\zeta(0) + A_1\zeta(-T), \tag{21}$$

and $\mathbf{F} : \mathcal{C} \to \mathbb{R}^2$ is a nonlinear function defined by

$$\mathbf{F}(\zeta(\sigma)) = \mathbf{f}(\zeta(0), \zeta(-T)). \tag{22}$$

Note that (20) admits the trivial solution $\mathbf{x}_t(\sigma) = 0,\ -T \le \sigma \le 0$, which corresponds to the equilibrium solution $\eta = \beta p_0$ of (4). The stability of this equilibrium solution can be studied via the linearization of (20)

$$\mathbf{x}'(t) = L(\mathbf{x}_t). \tag{23}$$

In particular, the trivial solution of (23) will be asymptotically stable (and hence the equilibrium solution of (4) will be locally asymptotically stable) if all the eigenvalues of the operator L have negative real parts. It can be shown [20] that the eigenvalues of

L correspond to the roots of the characteristic equation $\det[\lambda I - A_0 - A_1 e^{-\lambda T}] = 0$, which simplifies to

$$\Delta(\lambda) \overset{def}{=} \lambda^2 + (\gamma - \beta p_1)\lambda + (1 + \beta p_0) - \beta p_0 e^{-\lambda T} = 0. \tag{24}$$

Note that this may also be obtained by substituting the ansatz $\mathbf{x}(t) = \mathbf{k}e^{\lambda t}$ into (12) and looking for nontrivial solutions of the resulting vector-matrix equation.

Section 2 described curves, in the T, β parameter space, along which the equilibrium solution of (4) loses stability. At each point on these curves, the characteristic equation (24) has a pair of pure imaginary roots and the rest of the roots have negative real parts. It is straightforward to check that the FDE (20) satisfies the conditions for a Hopf bifurcation to occur as one passes through a point on these curves (see [20, pp. 331–333] for a statement of the Hopf bifurcation Theorem for FDEs). For example if β is increased with T fixed, the transversality condition may be checked by showing

$$\left.\frac{dRe(\lambda)}{d\beta}\right|_{\lambda=i\omega} = Re\left(\frac{d\Delta}{d\beta}\Bigg/\frac{d\Delta}{d\lambda}\right)\Bigg|_{\lambda=i\omega} \neq 0$$

at a point of one of the curves. The criticality of the Hopf bifurcation may be checked using a centre manifold approach as outlined below.

At a point where the characteristic equation (24) has a pair of pure imaginary roots and the rest of the roots have negative real parts, there exists a splitting of the solution space for the linear FDE (23) as $\mathcal{C} = N \oplus S$, where N is a two-dimensional subspace spanned by the solutions to (23) corresponding to the pure imaginary eigenvalues, S is infinite dimensional, and N and S are invariant under the flow associated with (23). It is straightforward to show that a basis for N is given by

$$\Phi(\sigma) = \begin{bmatrix} \cos(\omega\sigma) & \sin(\omega\sigma) \\ -\omega\sin(\omega\sigma) & \omega\cos(\omega\sigma) \end{bmatrix}. \tag{25}$$

N and S are analogous to the centre and stable eigenspaces for ODEs.

In this same situation, Hale and Lunel [20, Chapter 10] have shown that there exists, in the solution space $\mathcal{C}$ for the nonlinear FDE (20), a two-dimensional centre manifold. Since all other eigenvalues of L have negative real parts, this manifold is attracting and the long-term behaviour of solutions to the nonlinear equation is well approximated by the flow on this manifold. In particular, studying the flow on this manifold will enable us to determine the criticality of the Hopf bifurcation which occurs when the characteristic equation has a pair of pure imaginary roots. Below, we outline the steps involved in computing this manifold. The approach we will take follows the work of of Hale [19] and Wischert et al. [48] (scalar case) and of Faria and Magalhães [15], [16] (vector case).

To begin, we note that points on the centre manifold can be expressed as the sum of a linear part belonging to N and a nonlinear part belonging to S, i.e.,

$$M_f = \{\phi \in \mathcal{C} \mid \phi = \Phi\mathbf{u} + \mathbf{h}(\mathbf{u})\ ,\ \mathbf{h} \in S\}\ .$$

The solutions on this centre manifold are then given by

$$\mathbf{x}_t(\sigma) = \Phi(\sigma)\mathbf{u}(t) + \mathbf{h}(\sigma, \mathbf{u}(t))\ , \tag{26}$$

where $\Phi(\sigma),\ \sigma \in [-T, 0]$ is the basis for N given above.

To calculate the centre manifold, we need to express (20) as an extended equation for $\mathbf{x}_t(\sigma)$. This can be done as follows (see [20]):

$$\dot{\mathbf{x}}_t(\sigma) = \begin{cases} \frac{d}{d\sigma}[\mathbf{x}_t(\sigma)], & -T \le \sigma < 0 \\ \\ L[\mathbf{x}_t(\sigma)] + \mathbf{F}[\mathbf{x}_t(\sigma)], & \sigma = 0 \end{cases}, \tag{27}$$

where L and $\mathbf{F}$ are as above.

Substituting (26) into (27) yields

$$[\Phi(\sigma) + D_u\mathbf{h}(\sigma, \mathbf{u}(t))]\dot{\mathbf{u}}(t) = \begin{cases} \Phi(\sigma)B\mathbf{u}(t) + \frac{\partial \mathbf{h}}{\partial \sigma}, & -T \le \sigma < 0 \\ \\ \Phi(0)B\mathbf{u}(t) + \mathbf{F}[\Phi(\sigma)\mathbf{u}(t) \\ +\mathbf{h}(\sigma, \mathbf{u}(t))] + L[\mathbf{h}(\sigma, \mathbf{u}(t))], & \sigma = 0 \end{cases}, \tag{28}$$

where

$$B = \begin{bmatrix} 0 & \omega \\ -\omega & 0 \end{bmatrix}.$$

This coupled system must be solved for $\mathbf{u}(t)$ and $\mathbf{h}(\sigma, \mathbf{u}(t))$. As in [20], we define the following scalar product for (23):

$$\langle \psi, \phi \rangle = \sum_{j=1}^{2} \psi_j(0)\phi_j(0) + \beta \tilde{p}_0 \int_{-T}^{0} \psi_2(\xi + T)\phi_1(\xi)d\xi, \tag{29}$$

which can be used to define a linear system adjoint to (23). The linear operator of this adjoint system also has the eigenvalues $\pm i\omega$, and a basis for the solutions corresponding to these eigenvalues is given by $\Psi(s),\ s \in [0, T]$, where

$$\langle \Psi(s), \Phi(\sigma) \rangle = \mathbf{I}\,, \tag{30}$$

with $\mathbf{I}$ the 2×2 identity matrix. Straightforward calculations show that $\Psi(s)$ is given by

$$\begin{aligned} &\frac{2\omega^2}{D}\cos(\omega s) \\ &\quad\times\begin{bmatrix} (\gamma-\beta p_1)(\beta\tilde{p}_0+1)T+2\omega^2+(\gamma-\beta p_1)^2 & (\beta\tilde{p}_0+1-\omega^2)T+(\gamma-\beta p_1) \\ \omega[((\gamma-\beta p_1)^2-(\beta\tilde{p}_0+1)+\omega^2)T+\gamma-\beta p_1] & \omega[(\gamma-\beta p_1)T+2] \end{bmatrix} \\ &+\frac{2\omega^2}{D}\sin(\omega s) \\ &\quad\times\begin{bmatrix} \omega[(\beta\tilde{p}_0+1-\omega^2-(\gamma-\beta p_1)^2)T-(\gamma-\beta p_1)] & -\omega[(\gamma-\beta p_1)T+2] \\ (\gamma-\beta p_1)(\beta\tilde{p}_0+1)T+2\omega^2+(\gamma-\beta p_1)^2 & (\beta\tilde{p}_0+1-\omega^2)T+(\gamma-\beta p_1) \end{bmatrix}, \end{aligned} \tag{31}$$

where $\tilde{p}_0 = p_0\cos(\theta)$ and

$$\begin{aligned} D \;=\; &(5 + 2(\gamma - \beta p_1)T)\omega^4 + \big[\beta^2\tilde{p}_0^2T^2 + 2(\gamma - \beta p_1)(\beta\tilde{p}_0 + 1)T \\ &+2(\gamma - \beta p_1)^2 - 2(\beta\tilde{p}_0 + 1)\big]\omega^2 + 2\beta\tilde{p}_0 + 1. \end{aligned}$$

Taking the scalar product of (28) with $\Psi(s)$, and using the fact that $\langle \Psi(s), \mathbf{h}(\sigma, \mathbf{u}(t)) \rangle = 0$, gives a system of ODEs for $\mathbf{u}(t)$, namely,

$$\dot{\mathbf{u}}(t) = B\mathbf{u}(t) + \Psi(0)\mathbf{F}[\Phi(\sigma)\mathbf{u}(t) + \mathbf{h}(\sigma, \mathbf{u}(t))] \,. \tag{32}$$

Using (32) in (28) then yields a system of partial differential equations for $\mathbf{h}(\sigma, \mathbf{u})$, viz.

$$\begin{aligned} &D_u\mathbf{h}(\sigma, \mathbf{u})\,[B\mathbf{u} + \Psi(0)\mathbf{F}[\Phi(\sigma)\mathbf{u} + \mathbf{h}(\sigma, \mathbf{u})]] + \Phi(\sigma)\Psi(0)\mathbf{F}[\Phi(\sigma)\mathbf{u} + \mathbf{h}(\sigma, \mathbf{u})] \\ &\qquad = \begin{cases} \frac{\partial \mathbf{h}}{\partial \sigma}, & -T \le \sigma < 0 \\ L[\mathbf{h}(\sigma, \mathbf{u})] + \mathbf{F}[\Phi(\sigma)\mathbf{u} + \mathbf{h}(\sigma, \mathbf{u})], & \sigma = 0 \end{cases} \,. \end{aligned} \tag{33}$$

Thus, the evolution of solutions on the centre manifold is determined by solving (33) for $\mathbf{h}(\sigma, \mathbf{u})$ and then (32) for $\mathbf{u}(t)$. To solve (33), one uses a standard approach in centre manifold theory, namely, one assumes that $\mathbf{h}(\sigma, \mathbf{u}(t))$ may be expanded in power series in $\mathbf{u}$. Now, to determine the criticality of the Hopf bifurcation, one need only find the terms up to and including those that are $O(\|\mathbf{u}(t)\|^3)$ in (32). Thus we only need the terms that are $O(\|\mathbf{u}(t)\|^2)$ in the series for $\mathbf{h}$, viz.

$$\mathbf{h}(\sigma, \mathbf{u}(t)) = \begin{bmatrix} h^1_{11}(\sigma)u_1(t)^2 + h^1_{12}(\sigma)u_1(t)u_2(t) + h^1_{22}(\sigma)u_2(t)^2 \\ h^2_{11}(\sigma)u_1(t)^2 + h^2_{12}(\sigma)u_1(t)u_2(t) + h^2_{22}(\sigma)u_2(t)^2 \end{bmatrix} + O(\|\mathbf{u}(t)\|^3). \tag{34}$$

Substituting (34) into the first part of (33) and equating terms with like powers of u_1, u_2 yields the following system of ODEs for the $h^i_{jk}(\sigma)$:

$$\frac{d}{d\sigma}\begin{bmatrix} h^i_{11} \\ h^i_{12} \\ h^i_{22} \end{bmatrix} + \omega \begin{bmatrix} 0 & 1 & 0 \\ -2 & 0 & 2 \\ 0 & -1 & 0 \end{bmatrix} \begin{bmatrix} h^i_{11} \\ h^i_{12} \\ h^i_{22} \end{bmatrix} = \begin{bmatrix} 0 \\ (1-\omega^2)\frac{p_1}{p_0} \\ \omega(\beta p_2 + (\gamma - \beta p_1)\frac{p_1}{p_0}) \end{bmatrix} g^i(\sigma), \quad i = 1, 2, \tag{35}$$

where

$$\begin{aligned} g^1(\sigma) &= \omega(\Psi_{\mathbf{12}}(0)\cos(\omega\sigma) + \Psi_{\mathbf{22}}(0)\sin(\omega\sigma)), \\ g^2(\sigma) &= \omega^2(\Psi_{\mathbf{22}}(0)\cos(\omega\sigma) - \Psi_{\mathbf{12}}(0)\sin(\omega\sigma)). \end{aligned}$$

These are linear systems and are easily solved to find the general solutions for the $h^i_{jk}(\sigma)$ in terms of six arbitrary constants $C_1, C_2, C_3, C_4, C_5, C_6$. For example,

$$\begin{aligned} h^1_{22}(\sigma) \;=\; &\left((1-\omega^2)\frac{p_1}{2p_0}\Psi_{12}(0) - \frac{\omega}{3}\left(\beta p_2 + (\gamma - \beta p_1)\frac{p_1}{p_0}\right)\Psi_{22}(0)\right)\cos(\omega\sigma) \\ &+ \left((1-\omega^2)\frac{p_1}{2p_0}\Psi_{22}(0) + \frac{\omega}{3}\left(\beta p_2 + (\gamma - \beta p_1)\frac{p_1}{p_0}\right)\Psi_{12}(0)\right)\sin(\omega\sigma) \\ &- \frac{C_6}{2}\cos(2\omega\sigma) + \frac{C_5}{2}\sin(2\omega\sigma) + C_2. \end{aligned}$$

A similar procedure may be applied to the second part of (33) to obtain a set of six boundary conditions for the h^i_{jk}. Substituting in the general solutions for the h^i_{jk} and solving the resulting linear system yields the following expressions for the arbitrary constants:

$$\begin{bmatrix} C_1 \\ C_2 \\ C_3 \\ C_4 \\ C_5 \\ C_6 \end{bmatrix} = M^{-1} \begin{bmatrix} \omega^2[(2(\gamma - \beta p_1) - (1-\omega^2)\Psi_{12}(0))\frac{p_1}{2p_0} + \beta p_2] \\ \omega(1-\omega^2)\frac{p_1}{p_0} \\ 0 \\ 0 \\ \omega(1-\omega^2)\Psi_{22}(0)\frac{p_1}{2p_0} \\ 0 \end{bmatrix}, \tag{36}$$

where

$$M = \begin{bmatrix} \beta p_1 - \gamma & -1 & -\omega & \frac{1}{2}(\gamma - \beta p_1) & \omega(\gamma - \beta p_1)(1 + \frac{1-\omega^2}{\beta \tilde{p}_0}) & -\frac{3}{2} + 2\omega^2 - \frac{(!-\omega^2)^2}{\beta \tilde{p}_0} \\ 0 & 0 & \beta p_1 - \gamma & -2\omega & 3 - 4\omega^2 + 2\frac{(1-\omega^2)^2}{\beta \tilde{p}_0} & 2\omega(\gamma - \beta p_1)(1 + \frac{1-\omega^2}{\beta \tilde{p}_0}) \\ \beta p_1 - \gamma & -1 & \omega & -\frac{1}{2}(\gamma - \beta p_1) & -\omega(\gamma - \beta p_1)(1 + \frac{1-\omega^2}{\beta \tilde{p}_0}) & \frac{3}{2} + 2\omega^2 - \frac{(1-\omega^2)^2}{\beta \tilde{p}_0} \\ 0 & 0 & 1 & 0 & 0 & -2\omega \\ 1 & 0 & 0 & -\frac{1}{2} & -\omega & 0 \\ 1 & 0 & 0 & \frac{1}{2} & \omega & 0 \end{bmatrix}.$$

Substituting the expansion, (34), for $\mathbf{h}(\sigma, \mathbf{u})$ into the ODEs (32) and using the definition of $\mathbf{F}$, (22) and (22), gives a system of ODEs describing the evolution in time of $\mathbf{u} = (u_1, u_2)$:

$$\begin{matrix} \dot{u}_1 = \omega u_2 + \Psi_{12}(0)(f_{11}u_1^2 + f_{12}u_1u_2 + f_{22}u_2^2 + f_{111}u_1^3 + f_{112}u_1^2u_2 + f_{122}u_1u_2^2 + f_{222}u_2^3) \\ \dot{u}_2 = -\omega u_1 + \Psi_{22}(0)(f_{11}u_1^2 + f_{12}u_1u_2 + f_{22}u_2^2 + f_{111}u_1^3 + f_{112}u_1^2u_2 + f_{122}u_1u_2^2 + f_{222}u_2^3) \end{matrix} + O(\|\mathbf{u}\|^4). \tag{37}$$

The f_{jk} and f_{ijk} are functions of the parameters β, T, γ, θ, p_0, p_1, p_2, the Hopf frequency ω, and the centre manifold coefficients $h^i_{jk}(0)$ and $h^i_{jk}(-T)$. For example,

$$\begin{aligned} f_{11} &= 0, \\ f_{12} &= \omega\beta p_1 \cos(\theta)(\cos(\omega T) - 1), \\ f_{22} &= \omega\beta(\omega p_2 - p_1 \cos(\theta)\sin(\omega T)), \\ f_{222} &= \beta[-\omega^2 p_2 \cos(\theta)\sin(\omega T) + (2\omega p_2 - p_1\cos(\theta)\sin(\omega T))h^2_{22}(0) \\ &\qquad + \omega p_1 \cos(\theta)(h^1_{22}(-T) - h^1_{22}(0))], \end{aligned}$$

with

$$h^1_{22}(0) = (1-\omega^2)\frac{p_1}{2p_0}\Psi_{12}(0) - \frac{\omega}{3}\left(\beta p_2 + (\gamma - \beta p_1)\frac{p_1}{p_0}\right)\Psi_{22}(0) - \frac{C_6}{2} + C_2,$$

etc. As should be expected, (37) is an ODE at a Hopf bifurcation. The criticality of this bifurcation (and hence of the Hopf bifurcation in the original system of DDEs) may be determined by applying standard approaches such as that found in [18, p. 152].

Becuase the algebra involved in the calculations described above is quite involved, we have implemented the procedure in the symbolic algebra language Maple [47]. Our algorithm is based on the work of [6], [9], [10].

References

[1] Altintas, Y., and E. Budak, *Analytical prediction of stability lobes in milling.* Annals of the CIRP **44**(1) (1995) 357–362.

[2] Bayly, P., Halley, J. E., Davies, M. A., and J. R. Pratt, *Stability analysis of interrupted cutting with finite time in cut.* ASME Publication MED-Vol. 11, Proceedings of the ASME Manufacturing Engineering Division (2000) 989–996.

[3] Bayly, P. V., S. A. Metzler, A. J. Schaut, and K. A. Young, *Theory of torsional chatter in twist drills: Model, stability analysis and comparison to test.* ASME J. Management Sci. & Eng. **123** (2001) 552–561.

[4] Bayly, P. V., K. A. Young, and J. E. Halley, *Analysis of tool oscillation and hole roundness error in a quasi-static model of reaming.* ASME J. Management Sci. & Eng. **123** (2001) 387–396.

[5] Bayly, P. V., M. T. Lamar, and S. G. Calvert, *Low frequency regenerative vibration and the formation of lobed holes in drilling.* ASME J. Management Sci. & Eng. **124** (2001) 275–285.

[6] Bélair, J., and S. A. Campbell, *Stability and bifurcations of equilibria in a multiple-delayed differential equation.* SIAM J. Appl. Math. **54** no. 5 (1994) 1402–1424.

[7] Bhatt, S. and C. Hsu, *Stability criteria for second order dynamical systems with time lag.* J. Appl. Mech. **33** (1966) 113–118.

[8] Campbell, S. A., *Stability and bifurcation in the harmonic oscillator with multiple delayed feedback loops.* Dyn. Cont. Disc. Impul. Sys. **5** (1999) 225–235.

[9] Campbell, S. A., and J. Bélair, *Analytical and symbolically assisted investigation of Hopf bifurcations in delay-differential equations.* Can. Appl. Math. Quart. **3** no. 2 (1995) 137–154.

[10] Campbell, S. A., J. Bélair, T. Ohira, and J. Milton, *Limit cycles, tori, and complex dynamics in second-order differential equations with delayed negative feedback.* J. Dyn. Diff. Eqs. **7** no. 1 (1995) 213–236.

[11] Campbell, S. A., J. Bélair, T. Ohira, and J. Milton, *Complex dynamics and multistability in damped harmonic oscillator with delayed negative feedback.* Chaos **5** no. 4 (1995) 640–645.

[12] Cooke, K., and Z. Grossman, *Discrete delay, distributed delay and stability switches.* J. Math. Anal. Appl. **86** (1982) 592–627.

[13] Ema, S., and E. Marui, *Suppression of chatter vibration in drilling.* J. Management Sci. & Eng. **120** (1998) 200–202.

[14] B. Ermentrout, *XPPAUT5.52 — The Differential Equations Tool*. Department of Mathematics, University of Pittsburgh, Pittsburgh, PA (2002).

[15] Faria, T., and L. Magalhães, *Normal forms for retarded functional differential equations with parameters and applications to Hopf bifurcation.* JDE **122** (1995) 181–200.

[16] Faria, T., and L. Magalhães, *Normal forms for retarded functional differential equations applications to Bogdanov-Takens singularity.* JDE **122** (1995) 201–224.

[17] Golubitsky, M., and W. F. Langford, *Classification and unfoldings of degenerate Hopf bifurcation.* JDE **41** (1981) 525–546.

[18] Guckenheimer, J., and P. Holmes, *Nonlinear Oscillation, Dynamical Systems, and Bifurcations of Vector Fields*. Springer-Verlag, New York (1983).

[19] Hale, J. K., *Flows on center manifolds for scalar functional differential equations*. Proc. Roy. Soc. Edinburgh **101A** (1985) 193–201.

[20] Hale, J. K., and S. M. Verduyn Lunel, *Introduction to Functional Differential Equations*. Springer-Verlag, New York (1993).

[21] Hsu, C., and S. Bhatt, *Stability charts for second-order dynamical systems with time lag.* J. Appl. Mech. **33** (1966) 119–124.

[22] Kalmár, T., G. Stépán, and F. Moon, *Subcritical Hopf bifurcation in the delay equation model for machine tool vibrations*. Nonlin. Dynam. **26** (2001) 121–142.

[23] Koenigsberger, F., and J. Tlusty, *Machine Tool Structures*, Vol. I. Pergamon Press, N.Y. (1970) p. 122.

[24] Longtin, A., and J. G. Milton, *Complex oscillations in the human pupil light reflex with mixed and delayed feedback.* Math. Biosci. **90** (1988) 183–199.

[25] Merchant, M. E., *Mechanics of the cutting process.* J. Appl. Phys. **16** 267 (1945).

[26] Milton, J. G., and A. Longtin, *Evaluation of pupil constriction and dilation from cycling measurements.* Vision Res. **30** (1990) 515–525.

[27] Minis, I., and R. Yanushevsky, *A new theoretical approach for the prediction of chatter in milling.* J. Eng. Ind. **115** (1993) 1–8.

[28] Moon, F. C., and M. A. Johnson, *Nonlinear dynamics and chaos in manufacturing processes. Dynamics and Chaos in Manufacturing Processes*, ed. F. C. Moon, Wiley, New York (1998) 3–32.

[29] Nayfeh, A. H., C.-M. Chin, and J. Pratt, *Perturbation methods in nonlinear dynamics—Applications of machining dynamics.* J. Man. Sci. Eng. **119** 4A (1997) 485–493.

[30] Oxley, P. L. B., *The Mechanics of Machining*. Ellis Horwood Ltd., Chincester (1989).

[31] Pratt, J., and A. H. Nayfeh, *Design and modeling for chatter control.* Nonlin. Dynam. **19** (1999) 49–69.

[32] Rincon, D. M., and A. J. Ulsoy, *Effects of drill vibrations on cutting forces and torques*. Annals of the CIRP **43** (1994) 59–62.

[33] Rincon, D. M., and A. J. Ulsoy, *Complex geometry, rotary inertia and gyroscopic moment effects on drill vibrations.* J. Sound & Vib. **188** (1995) 701–715.

[34] Shridar, R., R. E. Hohn, and G. W. Long, *A general formulation of the milling process equation.* Trans. ASME **79** (1957) 139–148.

[35] Shridar, R., R. E. Hohn, and G. W. Long, *A stability algorithm for the general milling process.* J. Eng. Ind. **90** (1968b) 330–334.

[36] Stépán, G., *Delay-differential equation models for machine tool chatter. Dynamics and Chaos in Manufacturing Processes*, ed. F. C. Moon, Wiley, New York (1998) 165–191.

[37] Stépán, G., *Retarded Dynamical Systems: Stability and Characteristic Functions*. Pitman Research Notes in Mathematics, Vol. 210. Longman Scientific and Technical, London (1989).

[38] Stephenson, D. A., and J. S. Agapiou, *Calculation of main cutting edge forces and torque for drills with arbitrary geometries.* Int. J. Machine Tools Man. **32** 4 (1992) 521–538.

[39] Stephenson, D. A., and S. M. Wu, *Computer models for the mechanics of three-dimensional cutting processes—Part II: Results for oblique end turning and drilling.* J. Eng. Ind. **110** (1988) 38–43.

[40] Stone, E., and A. Askari, *Nonlinear models of chatter in drilling processes.* Dynam. Sys. **17** no. 1 (2002) 65–85.

[41] Takens, F., *Unfoldings of certain singularities of vector fields: Generalized Hopf bifurcations.* JDE **14** (1973) 476–493.

[42] Tarng, Y. S., and T. C. Li, *Detection and suppression of drilling chatter.* J. Dyn. Sys. Meas. & Control **116** (1994) 729–734.

[43] Tarng, Y. S., and T. C. Li, *Adaptive recognition of drilling chatter.* J. Materials Proc. Tech. **48** (1995) 247–253.

[44] Tekinalp, O., and A. G. Ulsoy, *Modeling and finite element analysis of drill bit vibration.* ASME J. Eng. Ind. **111** (1989) 148–155.

[45] Tlusty, J., *The dynamics of high-speed milling.* J. Eng. Ind. **108** (1986) 59–67.

[46] Tobias, S. A., *Machine Tool Vibration*. Wiley, New York (1965).

[47] Waterloo Maple Software, *Maple 7*. University of Waterloo, Waterloo, Canada (2001).

[48] Wischert, W., A. Wunderlin, A. Pelster, M. Olivier, and J. Groslambert, *Delay-induced instabilities in nonlinear feedback systems.* Phys. Rev. E **49** no. 1 (1994) 203-219.